

## **INFORMATION TO USERS**

The most advanced technology has been used to photograph and reproduce this manuscript from the microfilm master. UMI films the text directly from the original or copy submitted. Thus, some thesis and dissertation copies are in typewriter face, while others may be from any type of computer printer.

The quality of this reproduction is dependent upon the quality of the copy submitted. Broken or indistinct print, colored or poor quality illustrations and photographs, print bleedthrough, substandard margins, and improper alignment can adversely affect reproduction.

In the unlikely event that the author did not send UMI a complete manuscript and there are missing pages, these will be noted. Also, if unauthorized copyright material had to be removed, a note will indicate the deletion.

Oversize materials (e.g., maps, drawings, charts) are reproduced by sectioning the original, beginning at the upper left-hand corner and continuing from left to right in equal sections with small overlaps. Each original is also photographed in one exposure and is included in reduced form at the back of the book. These are also available as one exposure on a standard 35mm slide or as a 17" x 23" black and white photographic print for an additional charge.

Photographs included in the original manuscript have been reproduced xerographically in this copy. Higher quality 6" x 9" black and white photographic prints are available for any photographs or illustrations appearing in this copy for an additional charge. Contact UMI directly to order.

# **U·M·I**

University Microfilms International  
A Bell & Howell Information Company  
300 North Zeeb Road, Ann Arbor, MI 48106-1346 USA  
313 761 4700 800 521-0600



**Order Number 9005718**

**Analysis and modeling of the long-term performance of  
amorphous photovoltaic arrays**

**Choi, Hong Kyu, Ph.D.**

**The University of Arizona, 1989**

**U·M·I**

**300 N. Zeeb Rd.  
Ann Arbor, MI 48106**



**ANALYSIS AND MODELING  
OF THE LONG-TERM PERFORMANCE OF  
AMORPHOUS PHOTOVOLTAIC ARRAYS**

by

**Hong Kyu Choi**

---

**A Dissertation Submitted to the Faculty of the  
DEPARTMENT OF NUCLEAR AND ENERGY ENGINEERING  
In Partial Fulfillment of the Requirements  
For the Degree of  
DOCTOR OF PHILOSOPHY  
WITH A MAJOR IN NUCLEAR ENGINEERING  
In the Graduate College  
THE UNIVERSITY OF ARIZONA**

**1 9 8 9**

THE UNIVERSITY OF ARIZONA  
GRADUATE COLLEGE

As members of the Final Examination Committee, we certify that we have read  
the dissertation prepared by Choi, Hong Kyu

entitled Analysis and Modeling of the Long-Term Performance of  
Amorphous Photovoltaic Arrays

and recommend that it be accepted as fulfilling the dissertation requirement  
for the Degree of PhD in Nuclear Engineering.

Paul Montross

14 Aug, 1989  
Date

David L Hettrich

14 Aug, 1989  
Date

John T. Pelt

14 Aug, 1989  
Date

\_\_\_\_\_

\_\_\_\_\_  
Date

\_\_\_\_\_

\_\_\_\_\_  
Date

Final approval and acceptance of this dissertation is contingent upon the  
candidate's submission of the final copy of the dissertation to the Graduate  
College.

I hereby certify that I have read this dissertation prepared under my  
direction and recommend that it be accepted as fulfilling the dissertation  
requirement.

Paul Montross  
Dissertation Director

14 Aug, 1989  
Date

**STATEMENT BY AUTHOR**

This dissertation has been submitted in partial fulfillment of requirements for an advanced degree at the University of Arizona and is deposited in the Library to be made available to borrowers under rules of the Library.

Brief quotations from this dissertation are allowable without special permission, provided that accurate acknowledgment of source is made. Requests for permission for extended quotation from or reproduction of this manuscript in whole or in part may be granted by the head of major department or the Dean of the Graduate College when in his or her judgment the proposed use of the material is in the interests of scholarship. In all other instances, however, permission must be obtained from the author.

SIGNED :

A handwritten signature in cursive script, appearing to read "Hongyan Chen", is written over a horizontal line.

**To my wife Heesun  
and our daughters  
Hyomin and Hyojin**

## ACKNOWLEDGEMENT

I would like to thank the faculty and staff of the Department of Nuclear and Energy Engineering for their help and support during my graduate education at the University of Arizona. I would especially like to express my sincere appreciation to Dr. David L. Hetrick who has been on committee in my examinations and has made valuable comments. I would also like to thank Dr. Robert L. Seale for his advice on the annealing experiment. Appreciation is also expressed to Dr. Rocco A. Fazzolari who has been my academic advisor for many years. Without his support and guidance, my graduate study would be impossible.

My deep sense of gratitude goes to my dissertation directors, Dr. Leland M. Montierth and Dr. John F. Peck. Without their patient guidance and encouragement, I could not have accomplished this work. I would also like to thank Dr. John Prince for his crucial advice at the beginning of this work, and Dr. Henry C. Perkins for his guidance and assistance in committee.

A special "thank you" goes to Mr. Donald Osborn at SERF for his help and friendship throughout this work. Mr. Danis Willet and Mr. David Wallerstein at ARCO Solar also provided me with information and experimental samples for this work. Mr. Raymond Bahm provided me with TMY data for Tucson. Their assistance facilitated this work.

Finally, I especially thank my wife and two daughters who have been a source of love, patience, and encouragement for many years. I also thank my family in my country for their understanding and support during my graduate study here.

## TABLE OF CONTENTS

	<u>Page</u>
LIST OF TABLES.....	8
LIST OF ILLUSTRATIONS.....	10
ABSTRACT.....	12
1. INTRODUCTION.....	14
1.1 Statement of the Problem.....	15
1.2 Previous Work on Long-Term Performance Analysis.....	16
1.3 Organization of the Dissertation.....	17
2. PREDICTION OF SOLAR RADIATION.....	19
2.1 Solar Location.....	20
2.2 Diffuse Solar Radiation Modeling.....	22
2.2.1 Hay's Model.....	24
2.2.2 Klucher's Model.....	24
2.2.3 Perez's Model.....	25
2.3 Typical Meteorological Year (TMY) Data.....	26
2.4 Modeling of Incident Solar Radiation.....	27
3. MODELING OF AMORPHOUS SOLAR CELL PERFORMANCE.....	31
3.1 Hydrogenated Amorphous Silicon Solar Cell.....	31
3.2 Thermal Model for Photovoltaic Cell Temperature.....	33
3.3 Electrical Performance Model of <i>a-Si:H</i> Photovoltaic Cell.....	39
3.4 Model Simulation of <i>a-Si:H</i> Performance.....	47
4. THE LIGHT-INDUCED DEGRADATION EFFECT.....	50
4.1 The Staebler-Wronski Effect.....	50
4.2 Analysis of the Degradation and Recovery of <i>a-Si:H</i> Solar Cells.....	54

**TABLE OF CONTENTS—continued**

	<u>Page</u>
4.3 Analysis and Modeling of <i>a-Si:H</i> Solar Cell Performance.....	61
5. EXPERIMENTAL METHODOLOGY AND RESULTS .....	68
5.1 Determination of <i>G</i> for Artificial Lamp .....	68
5.2 Experimental Methodology .....	72
5.3 Determination of <i>m</i> , $E_{ar}$ , and $k_r$ .....	76
5.4 Determination of $E_{ad}$ and $k_d$ .....	82
5.5 Correlation between Fill Factor and $\overline{\mu\tau}$ .....	88
5.6 Discussion.....	91
6. SIMULATION AND VALIDATION OF THE MODEL .....	93
6.1 Simulation of Insolation Incident on Photovoltaic Panel.....	93
6.2 Simulation of Photovoltaic Panel Temperature .....	94
6.3 Simulation of <i>I-V</i> Characteristics .....	98
6.4 Simulation of the SWE .....	98
6.5 Long-Term Performance Model .....	101
7. SUMMARY AND CONCLUSIONS .....	106
APPENDIX A: ASHRAE METHOD.....	108
APPENDIX B: COMPARISON OF EXPERIMENTAL AND CALCULATED PANEL TEMPERATURE .....	111
APPENDIX C: COMPARISON OF EXPERIMENTAL AND CALCULATED <i>I-V</i> CHARACTERISTICS .....	115
APPENDIX D: COMPARISON OF EXPERIMENTAL DEGRADATION DATA WITH CALCULATED DEGRADATION VALUES .	117
REFERENCES.....	121

## LIST OF TABLES

<u>Table</u>	<u>Page</u>
2.1 Monthly Solar Radiation, $Btu/ft^2$ .....	29
2.2 Analysis of Deviation .....	29
3.1 Monthly Averaged Daily Horizontal Radiation, $Btu/ft^2$	37
3.2 Monthly Averaged Clearness Index .....	38
3.3 Determination of Correlation Coefficient .....	42
3.4 Effect of Temperature and Light Intensity on $\Delta V_{oc}/\Delta I_{sc}$	44
3.5 Determination of the Maximum Power Points ARCO G4000 Experimental Data .....	46
3.6 Experimental and Simulated Maximum Power Points ....	48
4.1 $N_s(0)$ and $\overline{\mu\tau}_o$ of $\alpha$ -Si:H .....	56
4.2 Step-Size vs Accuracy .....	60
4.3 $l_{co}/d$ vs $I_{sc}$ .....	64
5.1 Measured Short-Circuit Currents .....	71
5.2 $I_{sc}$ divided by Light Intensity .....	72
5.3 Recovery in Short-Circuit Currents .....	77
5.4 Average Values for Percent Recovery in $I_{sc}$ at 300° F Annealing .....	79

LIST OF TABLES—continued

<u>Table</u>	<u>Page</u>
5.5 <i>RMSE</i> of the Best Sets of $E_{ar}$ and $k_r$ 2nd-order Reaction .....	80
5.6 <i>RMSE</i> of the Best Sets of $E_{ar}$ and $k_r$ 1st-order Reaction .....	80
5.7 Degradation in Short-Circuit Currents $1000\text{ W/m}^2$ & $50^\circ\text{F}$ .....	83
5.8 Degradation in Short-Circuit Currents $2000\text{ W/m}^2$ & $50^\circ\text{F}$ .....	83
5.9 <i>RMSE</i> of the Best Coincident Sets of $E_{ad}$ and $k_d$ .....	85
5.10 Degradation in Short-Circuit Currents $1000\text{ W/m}^2$ & $120^\circ\text{F}$ .....	86
5.11 <i>RMSE</i> of the Best Coincident Sets of $E_{ad}$ and $k_d$ $1000\text{ W/m}^2$ & $120^\circ\text{F}$ .....	86
5.12 Degradation Ratio in Fill Factor .....	88
5.13 Degradation Ratio in $\overline{\mu_T}$ .....	89
5.14 Evaluation of Correlation Model .....	90
6.1 Comparison of Degradation in Efficiency SERF vs Model .....	100
6.2 Comparison of Degradation in Efficiency Model vs Correlations .....	103
6.3 Electricity Generation, $\text{kWhr/m}^2$ .....	104

## LIST OF ILLUSTRATIONS

<u>Figure</u>	<u>Page</u>
2.1 Solar Angles on a Tilted Surface .....	21
2.2 Monthly Total Radiation on a Tilted Surface .....	30
3.1 Structure of Amorphous Silicon .....	33
3.2 Sky Temperature vs Clearness Index .....	38
3.3 Equivalent Circuits of Solar Cell Models .....	41
3.4 ARCO G4000 <i>I-V</i> Characteristics Curves .....	43
3.5 Output Power vs Voltage .....	45
4.1 Conductivity Change upon Light Exposure .....	51
4.2 Degradation of Efficiency vs Time and Temperature .....	53
4.3 <i>I-V</i> Characteristics of <i>a-Si:H</i> Before and After Light Exposure .....	53
5.1 Solar Spectral Distribution vs Air Mass .....	69
5.2 Spectral Collection Efficiency of <i>a-Si:H</i> .....	70
5.3 Experimental Apparatus .....	74
5.4 Percent Recovery vs Temperature .....	78
5.5 Percent Recovery at 300° <i>F</i> .....	79
5.6 Percent Recovery vs Annealing Reaction Order .....	81

LIST OF ILLUSTRATIONS—continued

<u>Figure</u>		<u>Page</u>
5.7	Percent Degradation at $1000\text{ W/m}^2$ & $50^\circ\text{ F}$ .....	84
5.8	Percent Degradation vs light Intensity .....	84
5.9	Degradation Effect vs Temperature .....	87
5.10	Comparison of Correlation at $1000\text{ W/m}^2$ & $50^\circ\text{ F}$ .....	90
6.1	Schematic of the Entire Model .....	94
6.2	Effect of Wind Speed on Panel Temperature .....	97
6.3	Effect of Initial Panel Temperature .....	97
6.4	Comparison of Degradation in Efficiency .....	100

## ABSTRACT

A validated predictive model of *a-Si:H* solar cell arrays was developed. The performance of *a-Si:H* solar cells was modeled by predicting the performance before degradation first, and then modifying it with terms that account for degradation and recovery effects.

A unique approach for the determination of the fundamental rate controlling parameters for the degradation and recovery process was carried out by observing the variation of the short-circuit current. By this approach, the analytical model became simple and the experimental measurement was easy.

The experimental annealing of *a-Si:H* silicon samples showed that the percent recovery from the degraded state to the as-grown state by annealing was virtually independent of the initial state at the start of the annealing process. This allowed the recovery parameters to be determined independently of the prior degradation process. Possible degradation parameters were determined at low temperatures. The best combination of degradation and recovery parameters was then determined from experiments where degradation and recovery occurred simultaneously.

An extremely simple and fast running algorithm for the long-term performance was developed in terms of the incident solar radiation, the panel temperature, and the total radiation exposed. Also it was found that the entire process of the Staebler-Wronski effect could be adequately represented by a correlation in which the degradation and recovery processes are solely a function of the total radiation

exposure of the panel at ambient conditions. These correlations were performed by manipulating the results obtained by the analytical and experimental study with the Programming Language for the Analysis of Economic Time Series (PLANETS) software.

The model generated results were validated with experimental data from the Solar Energy Research Facility (SERF) at the University of Arizona. The validation was satisfactory.

## CHAPTER 1

### INTRODUCTION

Photovoltaic cells are solid-state devices that absorb light and convert light energy directly into electricity. In the century and a half since the photovoltaic effect was first observed by French physicist Edmond Becquerel in 1839 (Angrist 1982), tremendous progress has been made in photovoltaic technology, especially in the thirty years following the first use of photovoltaic cells in the power supply of Vanguard I in 1958.

The emphasis of the research for space applications has been to develop more highly reliable, higher efficiency, and lighter weight photovoltaic cells which result in lower cost power for space, while terrestrial applications research has been directed toward lowering the cost of photovoltaic modules.

Thin film solar cells were developed in an attempt to reduce the cost of photovoltaic generation significantly. These include both amorphous silicon and polycrystalline thin film cells, which are about a hundred times thinner than crystalline cells. Amorphous silicon is a leading candidate among thin-film materials for the fabrication of flat-plate photovoltaic devices for electricity generation.

Spear and LeComber (1975) reported that amorphous silicon films produced by the glow discharge decomposition of silane ( $SiH_4$ ) could be doped to form *p-n* junctions. Using amorphous silicon-hydrogen alloys (*a-Si:H*) prepared in this way, a 5.5% efficient solar cell was reported (Carlson et al 1976). Recently, even for

100  $cm^2$  cells, efficiencies of greater than 9% have been reported (Shufflebotham and Card 1987).

The first commercial products based on amorphous silicon photovoltaic cells appeared in 1980. These cells were about 3% efficient in sunlight but matched the performance of single-crystal silicon cells under indoor fluorescent lighting. Since amorphous silicon photovoltaic cells require less than micron thicknesses of material and their processing is relatively simple, they have an initial market in light powered consumer products without batteries, which helps to fund their development.

### **1.1 Statement of the Problem**

Hydrogenated amorphous silicon ( $a-Si:H$ ) is a promising and rapidly advancing material for thin film solar cells. The performance of  $a-Si:H$  cells has been improved significantly in recent years. One of the major factors influencing the successful large-scale power source is maintaining long-term stable performance in an actual operating environment.

The substantial promise of amorphous silicon for large-scale and low-cost solar cells has resulted in a massive effort to understand and overcome the one remaining limitation of this material - its light induced degradation. The degradation effect was first observed by Staebler and Wronski (1977). Since then, the effect has received a considerable attention because it is directly related to the efficiency degradation of hydrogenated amorphous silicon ( $a-Si:H$ ) solar cells.

The goal of this study is to develop an analytical model for the prediction of the long-term performance and degradation of amorphous silicon photovoltaic arrays using typical meteorological year (TMY) data for Tucson. The model generated results will be validated with experimental data from the Solar Energy Research Facility (SERF) at the University of Arizona.

## 1.2 Previous Work for Long-Term Performance Analysis

Since the degradation effect was first observed, numerous theoretical and experimental studies for the long-term performance of amorphous silicon photovoltaic systems have been presented.

Staebler et al (1981) first reported the long-term performance tests of amorphous silicon *p-i-n* solar cells. The tests were conducted indoors using tungsten lamps. According to their experimental work, the conversion efficiency rapidly dropped, then was followed by a weak logarithmic decay. Extrapolation of the data to the equivalent of a 20 year exposure to sunlight resulted in efficiency degradation of 20%. They also pointed out that the efficiency degradation is mostly due to a decrease in the fill factor (the ratio of the maximum available power to the short-circuit current – the open-circuit voltage product) and the short-circuit current, while the open-circuit voltage changed only slightly.

Ullal et al (1984) investigated the stability of *a-Si:H* exposed to normal sunlight for a year. Their temperature studies clearly showed that degradation is reduced considerably when the cells operate at temperatures above the ambient temperature. They also proposed a model of efficiency degradation, representing initial rapid degradation and subsequent slow decay.

Hester and Hoff (1985) presented the long-term performance of photovoltaic modules with two and a half years of test data. The objective of the test was to evaluate the performance of the modules particularly in terms of degradation and to develop a database to be used for an engineering evaluation of the technology.

Ichikawa et al (1987) presented three year field tests of the degradation phenomena under different light intensities. They compared their experimental data with simulation studies by using accepted values of *a-Si:H* parameters in the

latter. They also pointed out that the degradation in continuous artificial light tests is much faster than that in the outdoor tests.

Sakai and Uchida (1987) also reported on the field test results of amorphous silicon solar cells exposed for one and a half years. They concluded that the two most noteworthy phenomena are the initial rapid degradation occurring within one month and the seasonal variation in the output performance.

Eser et al (1987) presented a long-term stability study of amorphous silicon solar cells. They analyzed coexisting light-induced degradation and thermal recovery processes and concluded that under normal operating conditions of 70 – 80°C, light-induced degradation is reduced due to simultaneous thermal recovery

Mrig et al (1987), DeBlasio et al (1987), and Mrig et al (1988) designed testing systems and analytical procedures for numerous thin-film modules and presented the test results based on long-term stability performance testing over the past two years. They also mentioned that new methods and procedures are currently under development in the Solar Energy Research Institute to evaluate and understand the degradation mechanisms and to influence future module design and fabrication for improved long-term stability.

From the review of prior work, it is quite clear that a predictive performance model for *a-Si:H* analysis which utilizes, synthesizes, and integrates fundamental information regarding solar and photovoltaic phenomena has not been written. The models and procedures discussed in this study were developed to meet this need.

### **1.3 Organization of the Dissertation**

Chapter 2 presents information regarding the prediction of solar incidence on a tilted surface using TMY data for Tucson. Anisotropic diffuse radiation models are reviewed and compared with the ASHRAE (American Society of Heating, Refrigerating, and Air conditioning Engineers)clear day model.

Chapter 3 reviews the nature of *a-Si:H* solar cells. The prediction models of cell temperature and electrical performance before degradation are discussed. The model generated results of *I-V* characteristics are compared with experimental data.

Chapter 4 reviews the degradation effect and prior studies for modeling the effect. Possible algorithms for characterizing the Staebler-Wronski effect and its effect on *I-V* characteristics which were developed in this study from prior work are discussed.

Chapter 5 presents the experimental procedures for the determination of the fundamental rate controlling parameters of degradation and recovery processes. Required empirical correlations are generated from experimental results using the PLANETS software.

Chapter 6 combines the models developed in prior chapters in a predictive computer model. The model generated results are validated with experimental data from the SERF.

Chapter 7 summarizes and discusses the results of this study.

## CHAPTER 2

### PREDICTION OF SOLAR RADIATION

The proper prediction of the available solar radiation incident on surfaces of various orientation is crucial for the design and performance analysis of solar energy conversion systems. Under clear sky conditions, the available solar radiation on surfaces can be predicted in purely empirical terms, since the solar-earth geometric relationships are repeated each year. Due to clouds, however, the prediction of insolation becomes very complicated due to the inherently chaotic nature of weather systems.

The total solar radiation incident on a tilted surface has three components: direct radiation, diffuse radiation, and ground-reflected radiation. The intensity of the ground-reflected radiation depends on the reflectivity of the ground and the tilt angle of the surface. This reflected component on a tilted surface, however, is not important except in the case of tilt angles close to  $90^\circ$  and a high ground reflectivity. For practical photovoltaic panels, the ground-reflected radiation is small enough to neglect. The diffuse radiation component, however, is too large to be neglected.

The sun's position in the sky and the amount of solar radiation incident on a tilted surface can be most conveniently expressed in terms of solar and geometric angles. Before discussing the diffuse component, a review of solar location is essential.

## **2.1 Solar Location**

The angles determined by the sun's position and the specific site are:

1. Solar zenith angle,  $\theta_z$
2. Solar altitude angle,  $\alpha$
3. Solar azimuth angle,  $\gamma_s$
4. Solar declination angle,  $\delta$
5. Solar hour angle,  $\omega$
6. Latitude angle,  $\phi$

The zenith angle is the angle subtended by a vertical line to the zenith and the line of sight to the sun. The altitude angle is the complementary angle of the zenith angle, therefore, it is the sun's angular distance from the horizon. The azimuth angle is the angular displacement from south of the projection of the direct radiation on the horizontal plane. The declination angle is the angular position of the sun at solar noon with respect to the plane of the equator. The hour angle is the angular displacement of the sun due to rotation of the earth on its axis at  $15^\circ$  per hour. The latitude angle is the angular location north or south of the equator.

The angles determined by the orientation of solar energy collecting surfaces on earth are:

1. Surface tilt angle,  $\beta$
2. Surface azimuth angle,  $\gamma$

The tilt angle indicates how far up from the horizontal a surface is sloped, while the surface azimuth angle denotes how the surface is positioned relative to the true north-south and east-west coordinates. Fig. 2.1 shows the solar angles on a tilted surface.



The above angles are combined together to yield the calculation of the angle of incidence,  $\theta$ . The angle of incidence,  $\theta$ , on any surface is defined as the angle between the direct radiation on a surface and the normal to that surface. Using the angle of incidence, the direct radiation component on a tilted surface can easily be calculated. The equation relating the angle of incidence and the other angles is

$$\cos \theta = \cos \delta \cos \phi \cos \beta (\tan \delta \tan \phi + \cos \omega) + \cos \delta \sin \beta \cos \gamma (\cos \omega \sin \phi + \sin \omega \tan \gamma - \tan \delta \cos \phi) \quad (2.4)$$

For the prediction of hourly total radiation incident on a tilted surface, the mean hour angle was used (TRNSYS 1983) in this study. This is to ensure that the calculated position of the sun will be the average position for the time interval. The mean hour angle,  $\omega_{mean}$ , is given by

$$\omega_{mean} = \frac{\omega_{initial} + \omega_{final}}{2} \quad (2.5)$$

At the mean hour angle, the incident solar radiation and the angle of incidence represent approximately the hourly average values of them.

## **2.2 Diffuse Solar Radiation Modeling**

The diffuse fraction of solar radiation is important for the prediction of solar radiation on a surface. Liu and Jordan (1960) first proposed that the ratio of daily diffuse to daily total radiation on a horizontal surface may be correlated with the sky clearness index in a location-independent manner. Although it is evident that a general correlation exists between the diffuse fraction and the clearness index, the data generally exhibit a relatively wide scatter and the resulting empirical relation are not in good agreement (Ma and Iqbal 1984). Smietana et al (1984) showed

that the diffuse radiation is not accurately determined by the clearness index alone. Suehrcke and McCormick (1988) concluded that next to the clearness index, the air mass is the second most important variable characterizing the instantaneous diffuse radiation.

Due to the variety and complexity of solar radiation, the diffuse radiation was simply assumed to be isotropic over the hemispherical sky (Liu and Jordan 1963). This assumption conveniently allows the direct and diffuse radiations on a horizontal surface to be corrected to the total radiation on a tilted surface by simple geometric relationships. For a surface of tilt  $\beta$  with the isotropic model, the diffuse radiation,  $I_{dt}$ , can be expressed as

$$I_{dt} = \frac{I_{dh}(1 + \cos \beta)}{2} \quad (2.6)$$

where  $I_{dh}$  is the diffuse radiation incident on a horizontal surface.

The isotropic model for the diffuse radiation is a good approximation for overcast skies, however, Dave (1977) showed that sky diffuse radiation is anisotropic in many instances and that the assumption of an isotropic distribution may introduce significant error in estimating the diffuse radiation on tilted surfaces. Since then, anisotropic models for diffuse radiation have been developed. Anisotropic models take into account the circumsolar radiation. The diffuse radiation is, therefore, composed of two parts, an isotropic and a circumsolar part that has the same angular time variations as the direct component from the sun.

Ma and Iqbal (1983) compared anisotropic models proposed by Hay (1979) and Klucher (1979) with the isotropic one and concluded that the two anisotropic models are definitely superior to the isotropic model for surfaces with tilt angles up to  $60^\circ$ . Perez et al (1986) developed an even better anisotropic model, and subsequently presented a simplified version of their improved model (Perez et al

1987). The three anisotropic models mentioned above will be explained in more detail.

### 2.2.1 Hay's Model

The diffuse radiation on a horizontal surface was expressed as a combination of a circumsolar component coming directly from the sun and an isotropically distributed diffuse component from the rest of the skydome. The hourly diffuse radiation on a tilted surface,  $I_{dt}$ , was written as

$$I_{dt} = I_{dh} \left[ \left( \frac{I_h - I_{dh}}{I_o} \right) \left( \frac{\cos \theta}{\cos \theta_z} \right) + \frac{(1 + \cos \beta)}{2} \left( 1 - \frac{I_h - I_{dh}}{I_o} \right) \right] \quad (2.7)$$

where  $I_{dh}$  is the diffuse radiation on a horizontal surface;  $I_h$  is the total horizontal radiation;  $I_o$  is the extraterrestrial radiation on a horizontal surface;  $\theta$  is the angle of incidence;  $\theta_z$  is the zenith angle.

The first term of the right hand side of eq. (2.7) accounts for the circumsolar and the second term for the isotropic component of the diffuse radiation. When overcast conditions prevail ( $I_h \approx I_{dh}$ ), Hay's model approaches the isotropic model.

### 2.2.2 Klucher's Model

Klucher modified the anisotropic clear day model developed by Temps and Coulson (1977) by adding a modulating function  $F$  as the sky varies from clear to overcast. The model takes into account the circumsolar radiation and the horizon brightening. The hourly diffuse radiation on a tilted surface,  $I_{dh}$ , is

$$I_{dt} = \frac{I_{dh}}{2} (1 + \cos \beta) \left[ 1 + F \sin^3(\beta/2) \right] (1 + F \cos^2 \theta \sin^3 \theta_z) \quad (2.8)$$

where

$$F = 1 - \left( \frac{I_{dh}}{I_h} \right)^2$$

The term  $[1 + F\sin^3(\beta/2)]$  accounts for the increase in diffuse radiation observed near the horizon during clear days, while the term  $(1 + F\cos^2\theta \sin^3\theta_z)$  represents the circumsolar effect. The modulating function  $F$  varies from 1 (very clear day,  $I_h \gg I_{dh}$ ) to 0 (overcast day,  $I_h = I_{dh}$ ). The Klucher model, however, fails to yield  $I_{dt} = I_{dh}$  for  $\beta = 0$ . Baltas et al (1986) added a correction factor by dividing the right side of eq. (2.8) by  $(1 + F\cos^2\theta_z \sin^3\theta_z)$ . Under overcast conditions, the Klucher model is equivalent to the isotropic model due to  $F = 0$ . When  $F$  approaches unity, the model approximates the Temps-Coulson anisotropic clear sky model.

### 2.2.3 Perez's Model

Perez et al (1987) proposed an anisotropic diffuse radiation model on tilted surfaces. According to their model, the diffuse radiation on tilted surfaces,  $I_{dt}$ , is

$$I_{dt} = I_{dh} \left[ (1 - F_1) \left[ \frac{(1 + \cos \beta)}{2} \right] + F_1 \frac{\cos[\min(\pi/2, \theta)]}{\cos \theta_z} + F_2 \sin \beta \right] \quad (2.9)$$

where  $F_1$  and  $F_2$  are the circumsolar and horizon reduced brightness coefficients;  $\theta$  is the incident angle;  $\theta_z$  is the zenith angle.

$F_1$  and  $F_2$  were derived by least square fitting of data as a function of three parameters of solar conditions: the solar zenith angle, the atmosphere clearness, and the atmosphere brightness. If  $F_1 = F_2 = 0$ , this model becomes the isotropic one. This is the most recent model for the prediction of the diffuse radiation. The model also was validated for several sites including Phoenix, AZ, and Albuquerque, NM. According to the model validation (Perez et al 1987), this model is more accurate than Hay and Klucher algorithms, especially for Phoenix and Albuquerque. The climatic conditions in Tucson may be similar to those in the two cities, therefore, the Perez model was chosen for the prediction of the diffuse radiation incident on

photovoltaic panels in this study. The Perez model also was satisfactory at Calgary and Alberta in Canada (Harrison and Coombes 1989).

### **2.3 Typical Meteorological Year Data**

While hourly total radiation on a horizontal surface is now recorded at many stations, stations measuring the hourly diffuse component are extremely few. Regardless of the diffuse model used, one has to know the diffuse radiation on a horizontal surface,  $I_{dH}$ . To meet this need, the typical meteorological year (TMY) data for Tucson was used as an hourly weather model in this study. From the TMY data, the direct normal radiation and the total horizontal radiation are available. The history and background of the TMY data were summarized by Bahm (1985).

For the United States, the hourly solar radiation on a horizontal surface has been measured for 26 cities around the country. Their 23-year data base form the SOLMET hourly data base. Then, it was extended to 222 additional locations, which had sunshine or cloud cover observations. The addition of direct normal radiation components was generated from a model, not measured.

The TMY data must be typical of the long-term weather data base and have a representative hourly picture of the climate of a year's duration. In spite of its inherent error due to the modeled direct normal radiation, the TMY data must be the most common hourly data set for the long-term performance analysis of photovoltaic systems if actual data are not available.

### **2.4 Modeling of Incident Solar Radiation**

When the direct normal radiation,  $I_{bn}$ , is known, the direct radiation falling on a horizontal surface,  $I_{bh}$ , can be calculated by

$$I_{bh} = I_{bn} \cos \theta_z \quad (2.10)$$

Then, the diffuse component on a horizontal surface,  $I_{dh}$ , can be found by subtracting the direct horizontal radiation,  $I_{bh}$ , from the total horizontal radiation,  $I_h$ .

$$I_{dh} = I_h - I_{bh} \quad (2.11)$$

The diffuse radiation on a tilted surface,  $I_{dt}$ , then can be calculated by the Perez algorithm in eq. (2.9). The direct radiation on a tilted surface,  $I_{bt}$ , can be obtained from the direct normal radiation and the incident angle,  $\theta$ , to the surface.

$$I_{bt} = I_{bn} \cos \theta \quad (2.12)$$

The total radiation on a tilted surface,  $I_{tt}$ , can be found by adding the direct radiation on a tilted surface,  $I_{bt}$ , to the diffuse radiation on a tilted surface,  $I_{dt}$ .

$$I_{tt} = I_{bt} + I_{dt} \quad (2.13)$$

Based on the calculational procedures described above, the prediction of solar radiation incident on a tilted surface was performed by the following:

1. Compute the mean hour angle for the time step from eq. (2.5).
2. Compute the solar zenith angle from eq. (2.2).
3. Compute the angle of incidence from eq. (2.4) using solar angles.
4. Compute the direct radiation falling on a horizontal surface from eq. (2.10).

5. Compute the diffuse radiation on a horizontal surface from eq. (2.11).
6. Compute the direct radiation incident on a tilted surface from eq. (2.12).
7. Compute the diffuse radiation on a tilted surface by the Perez model in eq. (2.9).
8. Compute the total radiation incident on a tilted surface from eq. (2.13).

The photovoltaic panel in this study has a  $32^\circ$  tilt angle and faces due south in Tucson. The results of the monthly total solar radiation calculated by the three anisotropic diffuse radiation models and the ASHRAE method (ASHRAE Handbook of Fundamentals 1981, see Appendix-A) are shown in Table 2.1 and graphically in Fig. 2.2. The ASHRAE model, which is designed for clear days, was not used for the prediction of solar radiation in this study. However, the model provides the maximum possible solar radiation on a surface, thereby it was used to check the simulation results of other models.

According to the results, the Klucher model performs very much like the Perez model. The Hay model agrees well with the other two anisotropic models from March to September, however, the Hay model deviates much for the rest of the year. Table 2.2 shows the relative error and the root mean square error (*RMSE*) with respect to the Perez model.

Table 2.1 Monthly Solar Radiation, *Btu/ft<sup>2</sup>*

Month	ASHRAE	Hay	Klucher	Perez
Jan	61411	51036	48536	48896
Feb	60893	54384	51563	52449
Mar	72912	67204	65541	66447
Apr	74263	70825	70559	71906
May	74900	72596	73440	74249
Jun	70409	67903	68996	69459
Jul	73818	61984	62607	63369
Aug	74014	64140	64186	65680
Sep	70199	64699	63700	64930
Oct	68627	67619	63733	63837
Nov	61368	53842	51363	51903
Dec	59738	50533	47615	47346
Total	822552	746765	731839	740471

Table 2.2 Analysis of Deviation

Month	Hay	Klucher
Jan	4.38%	-0.74%
Feb	3.69%	-1.69%
Mar	1.14%	-1.36%
Apr	-1.50%	-1.87%
May	-2.23%	-1.09%
Jun	-2.24%	-0.67%
Jul	-2.19%	-1.20%
Aug	-2.34%	-2.27%
Sep	-0.36%	-1.89%
Oct	5.92%	-0.16%
Nov	3.74%	-1.04%
Dec	6.73%	0.57%
<i>RMSE</i>	3.55%	1.36%

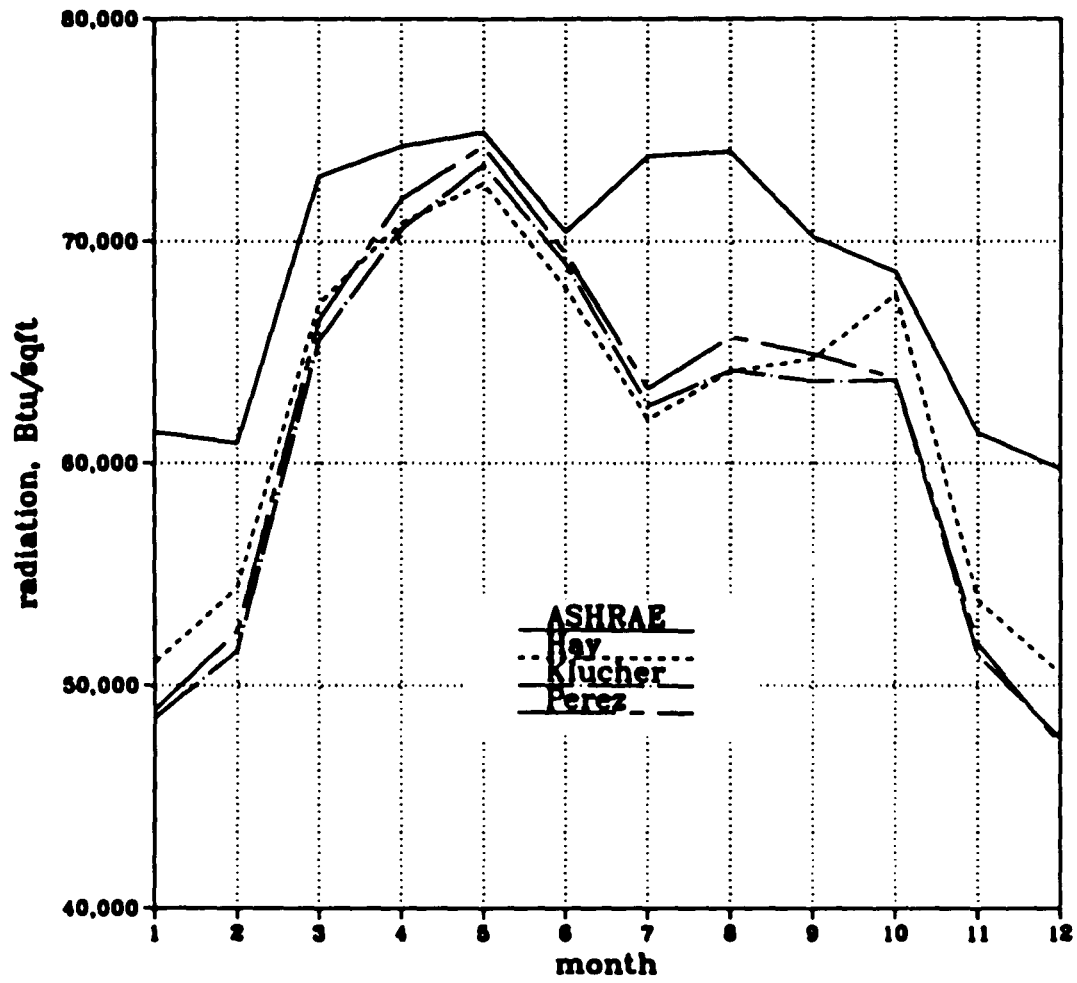


Fig. 2.2 Monthly Total Radiation on a Tilted Surface

Tilt angle: 32°; Orientation: due South

## CHAPTER 3

### MODELING OF AMORPHOUS SOLAR CELL PERFORMANCE

The amorphous semiconductor is a whole new class of materials for making solar cells. Amorphous thin film and crystalline photovoltaic cells are fabricated in entirely different ways and are fundamentally different in nature.

In this chapter, the nature of hydrogenated amorphous silicon solar cell ( $a\text{-Si:H}$ ) will be briefly reviewed first. For the prediction of the performance of  $a\text{-Si:H}$ , a thermal model for the calculation of photovoltaic cell temperature will be presented. Then, the modeling of  $I$ - $V$  characteristics of  $a\text{-Si:H}$  without degradation will be discussed.

#### 3.1 Hydrogenated Amorphous Silicon Solar Cell

An amorphous material is one that has no long-range crystalline structure, while appearing to be solid. Glass is a good example of such a material. For crystals, there is a strict periodicity. The periodicity is referred to as long-range order. In the case of amorphous solids, only the short-range order remains. Like the tetrahedrally bonded array of crystalline silicon lattices, silicon atoms in amorphous silicon are generally connected to four other silicon atoms.

Without the constraints of periodicity, however, it is difficult for every silicon atom to be linked up with four others. In amorphous solids, therefore, some lattices are distorted. Some silicon atoms only have covalent bonds with three

surrounding silicon atoms, where the fourth bond is not formed. This defect causes a breakdown in long-range order and leads to an increase in the strain of the lattice. This unsaturated bond is referred to as a dangling bond and can be understood as a strain relieving mechanism. The dangling bond creates an available energy level in the quantum energy gap of silicon (the "forbidden" gap) with the unfortunate consequences discussed later.

In *a-Si:H*, hydrogen atoms play an important role. They terminate the dangling bonds by sharing their electrons with the dangling electrons of the silicon. By doing so, the defect states within the forbidden gap can be removed. In pure *a-Si*, there are more than  $10^{19} \text{cm}^{-3}$  defects, while for *a-Si:H*, there are three to four orders of magnitude fewer defects. Therefore, hydrogen atoms dramatically improve the electrical and optical properties of the material.

Although hydrogen can saturate most of the silicon dangling bonds in *a-Si*, there are still typically about  $5 \times 10^{15} \text{cm}^{-3}$  dangling bond states in the gap, which play important roles as effective recombination centers and are related to the light-induced changes in the material which degrade amorphous photovoltaic cell performance. Figure 3.1 schematically shows the structure of amorphous silicon. This figure also illustrates the concept of the dangling bonds and how hydrogen deactivates them.

The *a-Si:H* solar cells have *p-i-n* structures. The intrinsic layer (*i*-layer) is located between highly doped *p* and *n* layers, and is much thicker than the other layers (about 20 to 30 times). Most free carriers are generated in the *i*-layer. Also, the carrier loss through recombination in this layer is the most fundamental factor for current and voltage losses. The *i*-layer, therefore, is the critical location for the photovoltaic effect of *a-Si:H*. The efficiency of the solar cell also strongly depends on the electronic properties of the *i*-layer.

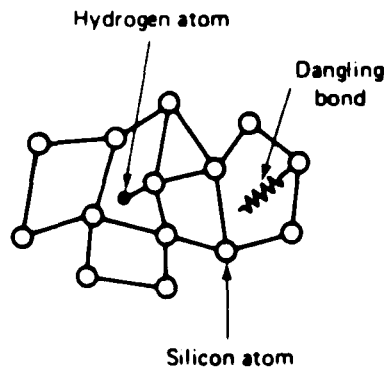


Fig. 3.1 Structure of Amorphous Silicon

The nature of  $a\text{-Si:H}$  was reviewed in this section. The prediction of photovoltaic cell temperature will be discussed in the next section.

### 3.2 Thermal Model for Photovoltaic Cell Temperature

It is well known that solar cell voltage and power are significantly influenced by cell temperature. Therefore, it is important to examine how cell temperature varies under different environmental conditions for the prediction of solar cell performance.

The daytime temperature of solar cells is significantly greater than the ambient temperature due to the absorption of insolation. During the day, a solar cell module operates at a temperature greater than the ambient temperature by a factor that depends on incident solar radiation, the absorptivity of the module, and mounting conditions. If solar cell modules are mounted in a way that facilitates convective cooling, they will operate at a lower temperature. For this reason, the wind

speed at a site strongly affects cell temperature and performance. Also, radiative heat transfer should be considered in ambient conditions.

Based on the phenomena mentioned above, Fuentes (1987) presented a simple model to calculate the uniform cell temperature. The model is capable of predicting the heat gain and the convective and radiative losses at any environmental condition, and also incorporates a thermal mass effect of a photovoltaic cell. According to the Fuentes model, the energy balance on a cell was expressed as

$$\alpha S = h_c(T_p - T_a) + \sigma \epsilon_c(T_p^4 - T_s^4) + \sigma \epsilon_g(T_p^4 - T_g^4) + mc \frac{dT_p}{dt} \quad (3.1)$$

where  $\alpha$  is the absorptivity of the cell;  $S$  is the incident solar radiation;  $h_c$  is the overall convective heat transfer coefficient;  $T_p$  is the cell temperature;  $T_a$  is the ambient temperature;  $\sigma$  is the Stefan-Boltzmann constant;  $\epsilon_c$  is the emissivity of the cell;  $T_s$  is the sky temperature;  $\epsilon_g$  is the emissivity of the ground;  $T_g$  is the ground temperature;  $mc$  is the thermal mass of the cell.

Equation (3.1) can be integrated and solved after linearizing the radiation terms as follows:

$$\sigma \epsilon_c(T_c^4 - T^4) = \sigma \epsilon_c(T_c^2 + T^2)(T_c + T)(T_c - T) = h_r(T_c - T) \quad (3.2)$$

where  $h_r$  is the radiative heat transfer coefficient. The product term  $(T_c^2 + T^2)(T_c + T)$  can be assumed constant because it does not change much in actual ambient conditions.

The model simulation procedure for cell temperature based on the Fuentes model will be explained in Chapter 6 and compared with actual experimental data for validation. In this section, the modification of the Fuentes model introduced in this study will be discussed. The modified portions are the calculation of convective heat transfer coefficients and the sky temperature.

Due to the chaotic nature of the environmental wind speed and direction, empirically derived expressions of the dimensionless numbers in heat transfer theory may not be applicable. Therefore, the dimensionless correlations used in the Fuentes model to determine convective heat transfer coefficients were replaced with a simplified ASHRAE correlation (ASHRAE Handbook of Fundamentals 1981) in this study. The correlation was originally developed for calculating cooling and heating loads in buildings.

$$h_c = 2 + \frac{4v}{15} \quad (3.3)$$

where  $v$  is the wind speed in miles per hour;  $h_c$  is in  $Btu/hr-ft^2-^{\circ}F$

The prediction of the sky temperature depends on the ambient temperature, humidity, amount of cloud cover, and elevation. Swinbank (1963) proposed a simple sky temperature equation for clear sky conditions by averaging out the effects of humidity and elevation on the sky temperature as follows:

$$T_s = 0.0552 \times T_a^{1.5} \quad (3.4)$$

where  $T_a$  and  $T_s$  are both in  $^{\circ}K$ .

Equation (3.4), however, is not applicable for cloudy days. During overcast days, the sky temperature is close to that of ambient. Therefore, the actual sky temperature would be somewhere between ambient temperature and the value obtained by eq.(3.4). In order to correlate the sky temperature to cloud conditions, the clearness index is the most appropriate approach. To modify eq.(3.4) under actual weather conditions, the following assumptions were made:

1. During overcast days,  $T_s = T_a$ .
2. On clear days,  $T_s = 0.0552 \times T_a^{1.5}$ .

3. Between the extreme conditions, the sky temperature linearly depends on the clearness index.

The clearness index was first proposed by Liu and Jordan (1960) and is defined as the ratio of the radiation on a horizontal surface to the extraterrestrial radiation on a horizontal plane. Depending upon the time step, the clearness index has the hourly, daily, and monthly averaged values. For simplicity, the monthly average was used in this study. The monthly average clearness index,  $\bar{K}_T$ , can be expressed as

$$\bar{K}_T = \frac{\sum H}{\sum H_o} \quad (3.5)$$

where  $\sum H$  is the monthly horizontal solar radiation;  $\sum H_o$  is the monthly extraterrestrial solar radiation on a horizontal plane. The extraterrestrial solar radiation incident on a horizontal plane,  $H_o$ , is (Duffie and Beckman 1980)

$$H_o = G_{sc} \left[ 1 + 0.033 \cos \left( \frac{360n}{365} \right) \right] \sin \alpha \quad (3.6)$$

where  $G_{sc}$  is the solar constant at  $428 \text{ Btu/hr-ft}^2$ ;  $n$  is the day of the year;  $\alpha$  is the solar altitude angle. If the ASHRAE clear day model is assumed, the monthly average clearness index on clear days,  $\bar{K}_{T,ash}$ , can be expressed by

$$\bar{K}_{T,ash} = \frac{\sum H_{ash}}{\sum H_o} \quad (3.7)$$

where  $\sum H_{ash}$  is the monthly solar radiation on a horizontal surface by the ASHRAE clear day model.

In order to estimate the clearness index on overcast days, typical overcast days in Tucson were identified in the TMY data month by month. From this data, the daily average horizontal radiation on overcast days,  $\sum H_{oc}$ , and the daily

average extraterrestrial radiation on a horizontal plane,  $\sum H_o$ , were calculated for each month. Then, the monthly average clearness index on overcast days,  $\bar{K}_{T,oc}$ , can be calculated from

$$\bar{K}_{T,oc} = \frac{\sum H_{oc}}{\sum H_o} \quad (3.8)$$

With the assumptions made above, the actual sky temperature,  $T_{s,act}$ , can be expressed as

$$\frac{T_{s,act} - T_a}{\bar{K}_T - \bar{K}_{T,oc}} = \frac{0.0552 \times T_a^{1.5} - T_{s,act}}{\bar{K}_{T,ash} - \bar{K}_T} \quad (3.9)$$

Rearranging eq. (3.9) for  $T_{s,act}$  gives

$$T_{s,act} = \frac{(\bar{K}_{T,ash} - \bar{K}_T)T_a + (\bar{K}_T - \bar{K}_{T,oc})(0.0552 \times T_a^{1.5})}{\bar{K}_{T,ash} - \bar{K}_{T,oc}} \quad (3.10)$$

Table 3.1 shows the monthly averaged daily horizontal radiation for different weather conditions. Table 3.2 depicts the corresponding monthly average clearness indexes for clear days, actual days, and overcast days in Tucson.

Table 3.1 Monthly Averaged Daily Horizontal Radiation,  $Btu/ft^2$

Month	Extraterrestrial	Clear	Actual	Overcast
Jan	1711	1262	1059	635
Feb	2069	1579	1384	950
Mar	2651	1996	1851	989
Apr	3112	2442	2353	1466
May	3465	2682	2675	1643
Jun	3567	2769	2701	1409
Jul	3487	2724	2297	1231
Aug	3175	2463	2166	1130
Sep	2803	2094	1935	872
Oct	2237	1687	1615	797
Nov	1791	1349	1180	686
Dec	1598	1170	995	644

Table 3.2 Monthly Averaged Clearness Index

Month	Clear	Actual	Overcast
Jan	.737	.619	.371
Feb	.763	.669	.459
Mar	.753	.698	.373
Apr	.785	.756	.471
May	.774	.772	.474
Jun	.776	.757	.395
Jul	.781	.659	.353
Aug	.776	.682	.356
Sep	.747	.690	.311
Oct	.754	.722	.356
Nov	.753	.659	.383
Dec	.732	.623	.403
Average	.761	.692	.392

Figure 3.2 provides the graphical view of eqn (3.10) and illustrates the location of the sky temperature under the different weather conditions. The sky temperature must lie on a straight line between state 1 and state 2, at a point which is proportional to the clearness index.

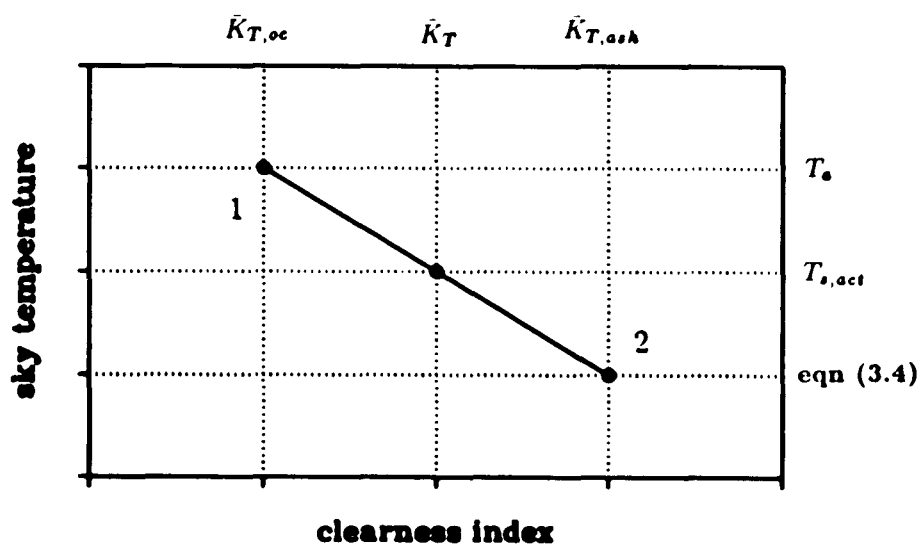


Fig. 3.2 Sky Temperature vs Clearness Index

In this section, the Fuentes model was introduced. Also, the modifications for the prediction of heat transfer coefficients in eq. (3.3) and the sky temperature in eq. (3.10) were discussed. The two equations will be used for the simulation model of *a-Si:H* cell temperature in Chapter 6.

In the next section, the electrical performance model will be discussed. The electrical performance of photovoltaic cells is determined by cell temperature and the amount of solar radiation incident on a cell surface.

### **3.3 Electrical Performance Model of *a-Si:H* Photovoltaic Cell**

In spite of the entirely different fabrication processes and the fundamental differences in the organization of their atoms, many similarities in electrical characteristics exist between crystalline and amorphous solar cells because of the short range order which determines these electrical properties. In most respects, the phenomena which determine the *I-V* characteristics of amorphous silicon solar cells are the same as those of crystalline solar cells (Hart 1986). These characteristics are:

1. Power varies approximately directly with incident solar radiation.
2. Current varies directly with incident solar radiation.
3. Voltage remains fairly constant relative to varying solar radiation.

The *a-Si:H* *I-V* characteristics differ significantly from crystalline solar cells in the two following ways (Hamakawa 1985; Hart 1986):

1. Existence of a high electric field in the carrier generation region in *a-Si:H*, therefore, the drift-type photovoltaic effect in *a-Si:H* dominates.
2. The fill factor of crystalline silicon is typically 0.75-0.80, while *a-Si:H* is in the range of 0.5-0.6.

With the similarities between crystalline and amorphous solar cells, the solar cell equation for a single diode model is well behaved for amorphous silicon solar cells (Czubatyj et al 1980; Kuwano et al 1981; Dressnandt and Rothwarf 1984; Mitchell et al 1985).

To date, no single solar cell model exists which accurately simulates all available solar cells over a wide ranges of temperatures, solar intensity, and other environmental effects. The most widely used model is the single diode model which is derived from solid-state theory and observations made on the solar cell terminal characteristics under different test conditions. The ideal solar cell equation derived from solid-state theory is

$$I = I_L - I_D = I_L - I_o \left[ \exp\left(\frac{qV}{kT}\right) - 1 \right] \quad (3.11)$$

where  $I$  is the load current;  $I_L$  is the light-generated current;  $I_D$  is the diode current;  $I_o$  is the reverse saturation current;  $q$  is the electron charge;  $k$  is the Boltzmann constant;  $V$  is the load voltage;  $T$  is the cell temperature. The diode reverse saturation current,  $I_o$ , was assumed constant in this study. Since the value of the diode reverse saturation current density is in the range of  $1 - 3 \times 10^{-12}$  amps/cm<sup>2</sup> (Green 1982), the following value was used with cell surface area,  $A_c$ :

$$I_o = A_c \times 2 \times 10^{-12} \text{ amps}$$

Equation (3.11), however, is not accurate enough to use for the analysis of actual solar cell  $I$ - $V$  characteristics for engineering purposes. Therefore, the following three additional parameters are usually included in eq.(3.11) (Rauschenbach 1980):

1.  $A$ , diode quality factor (or diode imperfection factor).
2.  $R_s$ , series resistance.

### 3. $R_{sh}$ , shunt resistance.

With these additional parameters, eqn (3.11) is expressed as (Rauschenbach 1980)

$$I = I_L - I_o \left[ \exp \left[ \frac{q(V + IR_s)}{AkT} \right] - 1 \right] - \frac{V}{R_{sh}} \quad (3.12)$$

The equivalent circuits of the solar cell models in eqn (3.11) and eqn (3.12) are shown in Fig. 3.3. The left side is for eqn (3.11), and the right side is for eqn (3.12).

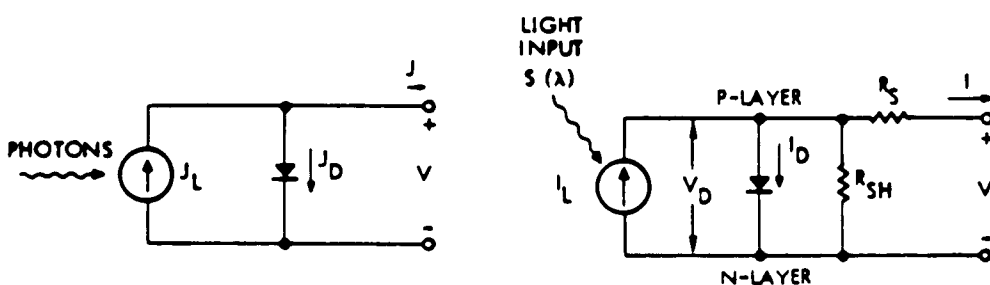


Fig. 3.3 Equivalent Circuits of Solar Cell Models

The term including shunt resistance,  $R_{sh}$ , in eqn (3.12) can be neglected because it is too small to affect the cell's behavior. Therefore, eqn (3.12) can be simplified as

$$I = I_L - I_o \left[ \exp \left[ \frac{q(V + IR_s)}{AkT} \right] - 1 \right] \quad (3.13)$$

The light-generated current,  $I_L$ , is relatively insensitive to cell temperatures and is directly proportional to incident solar radiation (Otterbein et al. 1978; Buresh 1983; Mitchell et al. 1985). Therefore, the light-generated current,  $I_L$ , at a given solar radiation,  $S$ , can be expressed as

$$I_L = I_{Lr} \frac{S}{S_r} \quad (3.14)$$

where  $I_{Lr}$  is the light-generated current at a reference solar radiation  $S_r$ .

Since  $I_L \approx I_{sc}$  (Araujo and Sanchez 1982), eq. (3.14) can be used for the calculation of  $I_{sc}$ .

$$I_{sc} = I_{Lr} \frac{S}{S_r} \quad (3.15)$$

Setting  $I = 0$  in eq. (3.13) with  $I_L (\approx I_{sc}) \gg I_o$ , the open-circuit voltage,  $V_{oc}$ , can be expressed by

$$V_{oc} = \frac{AkT}{q} \ln\left(\frac{I_{sc}}{I_o}\right) \quad (3.16)$$

A rise in cell temperature in eq. (3.16) appears to cause a proportional increase in the open-circuit voltage, which is not true. Thus, either  $A$  or  $I_o$  must change to reflect reality. While it may be more correct physically to allow  $I_o$  to be a function of temperature, this method is not used due to its complexity. Since the diode reverse saturation current,  $I_o$ , was assumed constant in this study, the temperature dependence of  $V_{oc}$  can be correctly expressed by making the diode quality factor,  $A$ , a function of temperature by the following equation:

$$A = A_r + C_A (T_r - T) \quad (3.17)$$

where  $A_r$  is the diode quality factor at a reference temperature,  $T_r$ ;  $C_A$  is the correlation coefficient and is  $\Delta A/\Delta T$ . From the G4000 specifications (ARCO 1988), the diode quality factor,  $A$ , has a value of 1.471 at 298°K. The correlation coefficient,  $C_A$ , was obtained using G4000 experimental data (see Fig. 3.4) and is shown in Table 3.3.

Table 3.3 Determination of Correlation Coefficient

Temperature °K	$V_{oc}$ volts	$A$	$C_A$ °K <sup>-1</sup>
298	0.852	1.4710	
333	0.756	1.1676	-0.00867

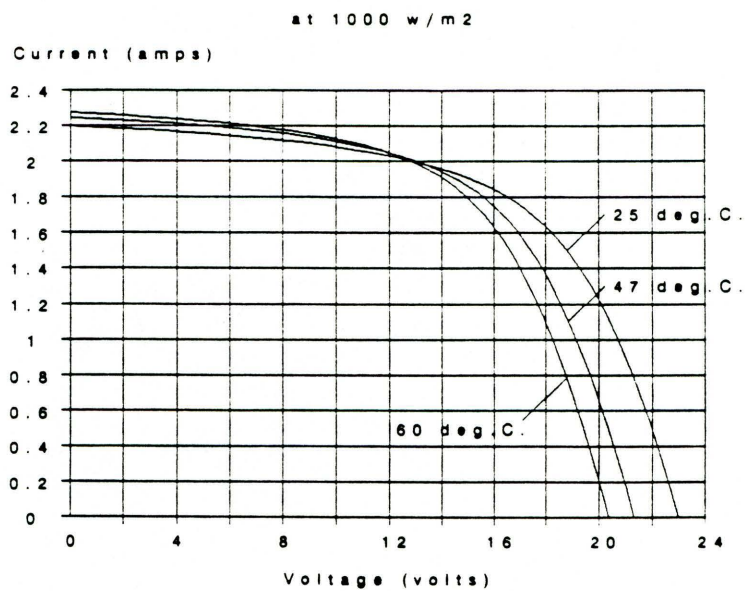
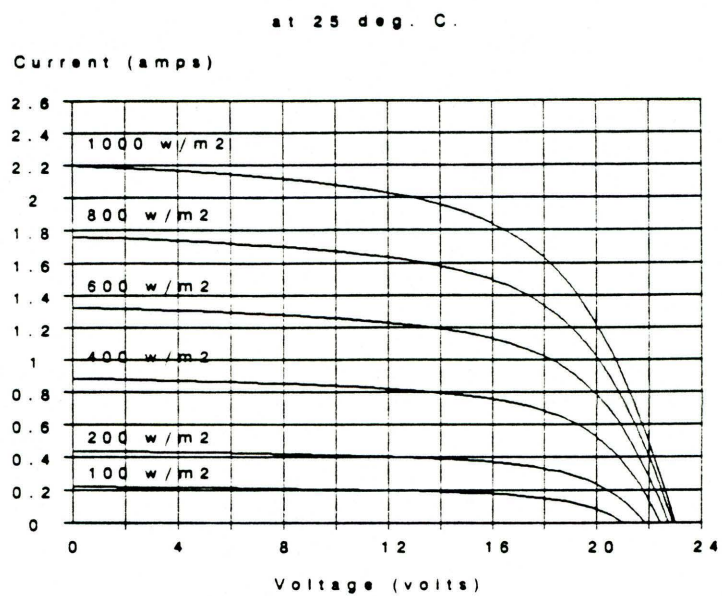


Fig. 3.4 ARCO G4000 *I-V* Characteristic Curves

The series resistance,  $R_s$ , of a solar cell is an idealization of internal electrical losses. The series resistance can be measured by observing the  $I$ - $V$  characteristics and varies with light intensity and temperature level. The preferred method of determining  $R_s$  experimentally uses the following equation (Rauschenbach 1980):

$$R_s = \frac{\Delta V_{oc}}{\Delta I_{sc}} \quad (3.18)$$

$\Delta V_{oc}$  and  $\Delta I_{sc}$  are determined from two  $I$ - $V$  curves from the same cell taken at different radiation levels, but the same temperature. The G4000  $I$ - $V$  characteristics were analyzed and Table 3.4 shows the temperature and light intensity dependence of  $\Delta V_{oc}/\Delta I_{sc}$  in eq. (3.18).

Table 3.4 Effect of Temperature and Light Intensity on  $\Delta V_{oc}/\Delta I_{sc}$

Solar $W/m^2$	Temperature $^{\circ}K$	$I_{sc}$ amps	$V_{oc}$ volts	$\Delta V_{oc}/\Delta I_{sc}$ ohms	Rad Effect	Temp Effect
1000	298	2.20	.852			
800	298	1.76	.848	.0082	0.00%	0.00%
600	298	1.32	.841	.0150	83.52%	0.00%
400	298	0.88	.827	.0323	295.84%	0.00%
1000	320	2.27	.785			
800	320	1.82	.781	.0081	0.00%	-0.68%
600	320	1.36	.775	.0142	75.00%	-5.29%
400	320	0.91	.761	.0304	275.00%	-5.67%
1000	333	2.30	.756			
800	333	1.84	.752	.0077	0.00%	-5.60%
600	333	1.38	.746	.0136	76.11%	-9.41%
400	333	0.98	.733	.0287	271.90%	-11.08%

From Table 3.4, the radiation dependence of  $\Delta V_{oc}/\Delta I_{sc}$  is much stronger than the temperature dependence. Taking average values of solar radiation and

$\Delta V_{oc}/\Delta I_{sc}$ , the following functional relation was obtained using least-square curve fitting for a straight line:

$$R_s = \frac{\Delta V_{oc}}{\Delta I_{sc}} = .056975 - .000056 S \quad (3.19)$$

As is expected, the series resistance decreases as light intensity increases due to the increasing density of light generated carriers.

By observation of the  $I$ - $V$  characteristics in Fig. 3.4, a particular pair of  $V_{oc}$  and  $I_{sc}$  will maximize the power output. This is called the maximum power point,  $P_m$ . The cell  $I$ - $V$  curve, therefore, passes through three significant points:  $I_{sc}$ , the short-circuit current;  $V_{oc}$ , the open-circuit voltage; and  $P_m$ , the maximum power point. Multiplying eqn (3.13) by  $V$ , the power,  $P$ , is written as

$$P = VI = VI_L - VI_o \left[ \exp \left[ \frac{q(V + IR_s)}{AkT} \right] - 1 \right] \quad (3.20)$$

Then, the maximum power,  $P_m$ , can be obtained by setting  $dP/dV = 0$ . Figure 3.5 shows the relation between output power and voltage.

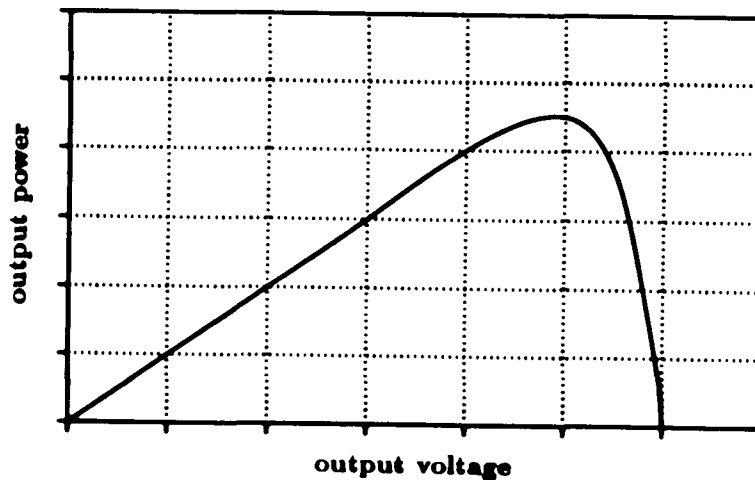


Fig. 3.5 Output Power vs Voltage

If the current is assumed to be fairly constant around the maximum power point with respect to the voltage change, the maximum power point can be expressed as

$$\frac{dP}{dV} = I_{sc} + I_o - I_o \exp\left[\frac{q(V_m + I_m R_s)}{AkT}\right] \left(\frac{AkT + qV_m}{AkT}\right) = 0 \quad (3.21)$$

where  $V_m$  and  $I_m$  are the voltage and current at the maximum power point, respectively. Rearranging eq. (3.21) for  $V_m$  leads to the following equation (Knobloch et al 1983):

$$V_m = \frac{AkT}{q} \ln\left[\left(\frac{I_{sc}}{I_o}\right) \left(\frac{AkT}{AkT + qV_m}\right)\right] - I_m R_s \quad (3.22)$$

If there is a relation between  $I_m$  and  $I_{sc}$ , eq. (3.22) can be solved by using eq. (3.15) and an initial guess of  $V_m$ . To derive this necessary relation, the maximum power points and the corresponding current values from G4000 experimental data were investigated and summarized in Table 3.5.

Table 3.5 Determination of the Maximum Power Points  
ARCO G4000 Experimental Data

Radiation $W/m^2$	voltage, volts				max power	$I_m/I_{sc}$
	16	17	18	20		
1000	29.28	29.75	25.74	24.40	29.75	.795
800	23.68	24.31	23.94	23.80	24.31	.813
600	18.08	18.70	18.54	15.60	18.70	.833
400	12.00	12.41	12.24	10.60	12.41	.830
200	5.92	5.95	5.94	4.60	5.95	.795
100	2.88	2.89	2.70	1.60	2.89	.773
average						.807

From the average value of  $I_m/I_{sc}$  in Table 3.5, the current at the maximum power point,  $I_m$ , at a different light intensity can be well approximated by

$$I_m = 0.807 \times I_{sc} \quad (3.23)$$

$V_m$  can be determined by iteration of eq. (3.22) with an initial guess of  $V_m$ . Then, the maximum power,  $P_m$ , is

$$P_m = I_m V_m \quad (3.24)$$

The fill factor,  $FF$ , is a measure of the squareness or sharpness of the knee in the  $I$ - $V$  curve and is defined by

$$FF = \frac{V_m I_m}{V_{oc} I_{sc}} = \frac{P_m}{V_{oc} I_{sc}} \quad (3.25)$$

The squarer the curve is, the greater the output power for a given  $I_{sc}$  and  $V_{oc}$ . The maximum conversion efficiency,  $\eta$ , can be found from

$$\eta = \frac{P_m}{S} = \frac{FF (V_{oc} I_{sc})}{S} \quad (3.26)$$

### **3.4 Model Simulation of $a$ -Si:H Performance**

Based on the procedures developed in the previous section, the model simulation for the prediction of  $a$ -Si:H performance was carried out by the following sequence:

1. Compute  $I_{sc}$  from eq. (3.15).
2. Compute  $V_{oc}$  from eq. (3.16).
3. Compute  $A$  from eq. (3.17).
4. Compute  $I_m$  from eq. (3.23).

5. Compute  $R_s$  from eq. (3.19).
6. Assume  $V_m$ . As an initial guess,  $V_m$  was assumed to be  $0.8 \times V_{oc}$ .
7. Compute  $V_m$  from eq. (3.22).
8. Compare the calculated  $V_m$  in step-7 with the assumed  $V_m$  in step-6.
9. If the difference between them is greater than the tolerance (0.05 V in this study), go to step-6 with the calculated  $V_m$  in step-7 as a second guess.
10. Repeat step-9 until the difference is within the tolerance.
11. Compute  $P_m$  and  $\eta$  from eq. (3.24) and eq. (3.26), respectively.

The experimental G4000 maximum power point and the simulated value are compared and summarized in Table 3.6 for various light intensities and cell temperatures.

Table 3.6 Experimental and Simulated Maximum Power Points  
( Cell temperature at 298° K )

Radiation $W/m^2$	G4000 <i>watts</i>	Model <i>watts</i>	Error
1000	29.75	31.97	7.46%
800	24.31	25.59	5.27%
600	18.70	19.21	2.73%
400	12.41	12.78	2.98%
200	5.95	6.30	5.88%
100	2.89	3.07	6.23%

( Radiation at 1000  $W/m^2$  )

Temperature $^{\circ}K$	G4000 <i>watts</i>	Model <i>watts</i>	Error
298	29.75	31.97	7.46%
320	28.01	29.68	5.97%
333	27.02	28.00	3.63%

The root mean square error (*RMSE*) of the model generated result is about 5%. Thus, the *I-V* characteristics model made in this study is satisfactory. In this chapter, the performance of *a-Si:H* was modeled and validated with experimental data. However, the degradation effect was not considered. The degradation effect will be discussed in the next chapter.

## CHAPTER 4

### THE LIGHT-INDUCED DEGRADATION EFFECT

The light-induced degradation in *a-Si:H* films was first observed by Staebler and Wronski (1977) and has been called the Staebler-Wronski effect (SWE). Since then, extensive research has been carried out in order to understand the origin and the operational mechanism of the light-induced defects because they are directly associated with the degradation of the efficiency of hydrogenated amorphous silicon (*a-Si:H*) solar cells. Although this effect has been well documented experimentally, no theoretical model has yet provided a comprehensive explanation of the observed phenomena.

In this chapter, the SWE and the previous studies for modeling the effect will be reviewed first. Possible models for the SWE and its effect on *I-V* characteristics developed from prior work in this study will be discussed.

#### 4.1 The Staebler-Wronski Effect

In 1977, Staebler and Wronski found that both the photoconductivity and the dark conductivity of intrinsic *a-Si:H* were significantly decreased when the samples were exposed to light in the range  $0.6 - 0.9 \mu m$  with the intensity of  $2000 W/m^2$  at room temperature. The results of the effect are shown in Fig. 4.1, which depicts the conductivity change as a function of time.

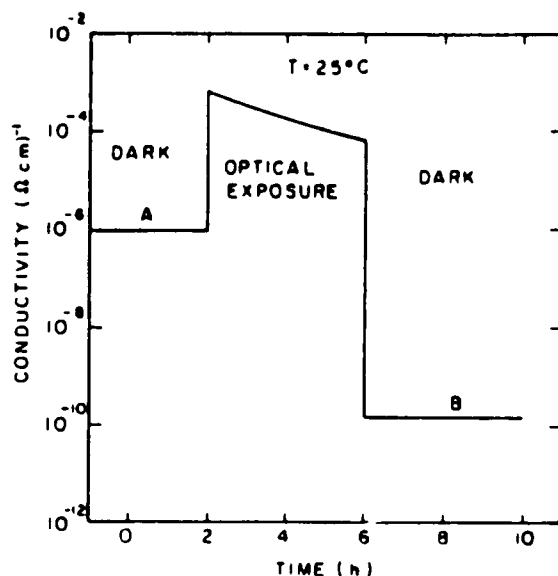


Fig. 4.1 Conductivity Change upon Light Exposure

For the first two hours before light exposure, the sample is in state-A and is held in the dark. During this period, the conductivity remains constant. When the light exposure first begins, the conductivity increases due to the electron-hole pairs generated by light. The rapid increase of the conductivity indicates the onset of the photoconductivity.

During the four hours of exposure, the photoconductivity decreases by a factor of 8. After the light is turned off, the dark conductivity in the degraded state (state-B) has dropped by nearly four orders of magnitude from its initial value in state-A. This new state is stable at room temperature, however, it is not an equilibrium state. The conductivity in state-B depends on the total light exposure that the sample received.

This effect is thermally reversible. The degraded samples can be returned to the initial state by annealing at  $150^\circ \text{C}$  in the dark for a few hours. The recovery

time is a function of annealing temperature. As the annealing temperature goes up, the recovery time required to return to the initial state goes down.

Staebler and Wronski concluded that the effect of light exposure is to increase the density of states in the energy gap, which can act as carrier recombination centers. Therefore, the observed photoconductivity decrease can be explained by a reduction in carrier lifetime. After their pioneering work, a number of studies have confirmed their conclusion about the reduction in carrier lifetime (Moller et al 1982; Swartz 1982; Uchida et al 1983; Tawada et al 1983; Faughnan and Crandall 1984; Smith et al 1985; Hack and Shur 1985; Bennett et al 1985; Yamaguchi et al 1987).

The accepted characteristics of the SWE from numerous experimental and theoretical studies can be summarized as follows and graphically in Fig. 4.2 and Fig. 4.3 (Staebler et al 1981; Nakano et al 1982; Tsuda et al 1983; Maruska et al 1983; Ullal et al 1984; Hack and Shur 1985; Lee et al 1985; Stutzmann et al 1985; Eser 1986; Bhargava et al 1987; DeBlasio et al 1987; Yanagisawa 1987; Mrig et al 1988):

1. The degradation in the efficiency is initially rapid but continually decreases as light exposure continues. The magnitude of light-induced degradation in the material decreases as the temperature increases. That means that the degradation and thermal recovery processes take place simultaneously during light exposure at elevated temperatures (Fig. 4.2).
2. The major loss of the efficiency is primarily due to the degradation in the fill factor. The open-circuit voltage remains fairly constant. A minor change in short-circuit current is also observed (Fig. 4.3).

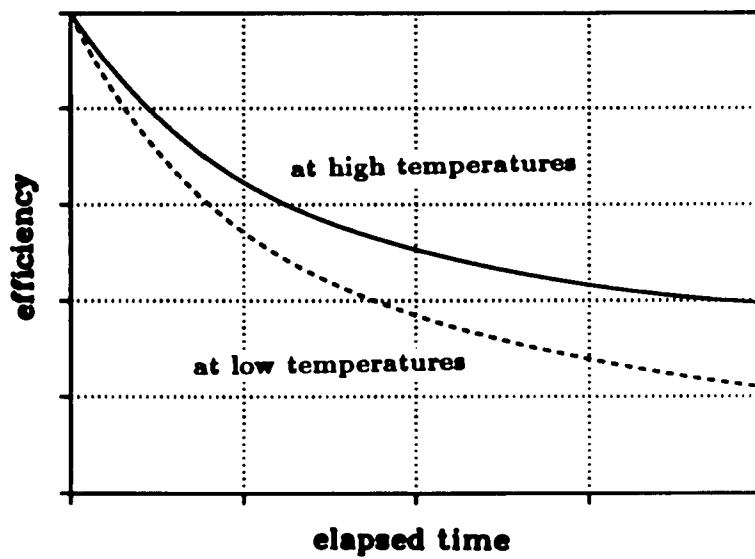
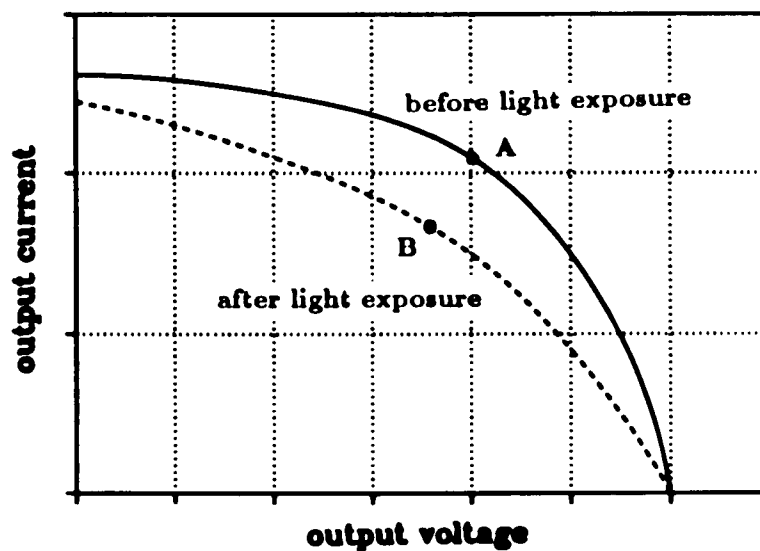


Fig. 4.2 Degradation of Efficiency vs Time and Temperature



A  $\rightarrow$  B: Light-induced degradation

B  $\rightarrow$  A: Thermal recovery by annealing

Fig. 4.3  $I$ - $V$  Characteristics of  $a$ - $Si:H$  Before and After Light Exposure

The exact mechanism of degradation is still not well understood. However, it is now believed that light-induced degradation in *a-Si:H* is the result of breaking the pre-existing stretched (weak) *Si:Si* bonds by the energy released from the band-to-band recombination of photo-generated electron-hole pairs. When a stretched *Si:Si* bond breaks, a dangling bond is formed. The stretched *Si:Si* bonds are, therefore, the sources for light-induced dangling bonds. The quantum energy of a dangling bond lies in the energy gap, thus facilitating recombination and lowering carrier lifetime. The dangling bond is dangling and not associated with a hydrogen atom. In one postulated recovery mechanism, hydrogen diffuses to the dangling bond and forms a covalent bond. Then the bond is not dangling any more. Another suggested recovery method invokes the reformation of a weak *Si:Si* bond from two adjacent dangling bonds (Eser 1986).

The SWE is intimately related to the reduction in carrier lifetime due to the increase in the dangling bond density. On the other hand, the change in carrier mobility,  $\mu$ , due to the degradation effect is quite small (Staebler and Wronski 1980). Yamagishi et al (1987) confirmed from their experiment that the effect of the mobility change is very minor compared to that of the lifetime change, which is important in the experimental work of this study. The quantitative analysis for the correlation between carrier lifetime and dangling bond density will be discussed in the next section.

#### **4.2 Analysis of the Degradation and Recovery of *a-Si:H* Solar Cells**

Numerous experimental models have been presented which quantitatively describe the degradation and recovery processes. In order to predict the degradation effect, the determination of degradation and recovery rates is quite essential. Prior work regarding modeling of the processes of degradation and recovery will

be reviewed in this section. Derivations performed in this study will be presented where appropriate.

The correlation between carrier lifetime and dangling bond density is crucial in this study. Smith et al (1985) postulated that the carrier lifetime is inversely proportional to the dangling bond density and proposed the following correlation:

$$\bar{\tau} = \left[ \bar{r} N_s(t) \right]^{-1} \quad (4.1)$$

where  $\bar{r}$  is the mean value of the coefficient of proportionality. Also, it is convenient to define a combined  $\mu\tau$  product of holes and electrons,  $\overline{\mu\tau}$ , because holes are in the minority on one side of the *i*-layer and electrons on the other side in a *p-i-n* solar cell (Smith et al 1985).

$$\overline{\mu\tau} = \mu_p \tau_p + \mu_n \tau_n \quad (4.2)$$

where  $\mu_p$  and  $\tau_p$  are the hole mobility and lifetime;  $\mu_n$  and  $\tau_n$  are the electron mobility and lifetime.

Since carrier mobility,  $\bar{\mu}$ , is relatively constant, carrier lifetime and dangling bond density were related through the following equation in this study:

$$\frac{\bar{\tau}_t}{\bar{\tau}_o} = \frac{\overline{\mu\tau}_t}{\overline{\mu\tau}_o} = \frac{\bar{r} N_s(0)}{\bar{r} N_s(t)} = \frac{N_s(0)}{N_s(t)} \quad (4.3)$$

where  $\bar{\tau}_o$  is the initial carrier lifetime before degradation. Equation (4.3) provides a means to correlate the dangling bond density with the carrier lifetime, which is an important relation in this study.

The initial values of the  $\overline{\mu\tau}$  product and dangling bond density before degradation must be known to use the correlation in eq. (4.3). The percent decrease in carrier lifetime then can be related to the percent increase in dangling bond density. Due to the unavailability of the experimental facilities, the initial dangling

bond density and the  $\overline{\mu\tau}$  product of the samples were obtained from the manufacturer and have the following typical values (Willet 1989):

$$N_s(0) = 5 \times 10^{15} \text{ cm}^{-3}$$

$$\overline{\mu\tau}_o = 2.0 \times 10^{-8} \text{ cm}^2 \text{ V}^{-1}$$

Accepted values of initial dangling bond density and  $\overline{\mu\tau}_o$  of *a-Si:H* before light exposure from previous studies are tabulated in Table 4.1.

Table 4.1  $N_s(0)$  and  $\overline{\mu\tau}_o$  of *a-Si:H*

Sources	$N_s(0), \text{ cm}^{-3}$
Street (1982)	$5 \times 10^{15}$
Lee et al (1985)	$5 \times 10^{15}$
Stutzmann et al (1985)	$10 \times 10^{15}$
Shepard et al (1988)	$3 \times 10^{15}$
Willet (1989)	$5 \times 10^{15}$

Sources	$\overline{\mu\tau}_o, \text{ cm}^2 \text{ V}^{-1}$
Street (1983)	$1.6 \times 10^{-8}$
Tawada et al (1983)	$3.0 \times 10^{-8}$
Xi et al (1985)	$2.8 \times 10^{-8}$
Yamaguchi et al (1987)	$3.0 \times 10^{-8}$
Willet (1989)	$2.0 \times 10^{-8}$

The most comprehensive studies of the rate of degradation and recovery were done by Stutzmann et al (1985), Lee et al (1985), and Eser (1986).

Stutzmann et al (1985) investigated the kinetics of degradation and recovery by photoconductivity and electron spin resonance (ESR) measurements. In their model, electrons and holes,  $n$  and  $p$ , are generated at a rate proportional to light intensity, while their densities are inversely proportional to the dangling bond density.

$$n = \frac{G}{r_n N_s} \quad (4.4)$$

$$p = \frac{G}{r_p N_s} \quad (4.5)$$

where  $G$  is the carrier generation rate;  $r_n$  and  $r_p$  are the recombination probabilities for electrons and holes through the energy levels associated with dangling bonds, respectively.

Under the assumption that new dangling bonds are created by the energy released from the band-to-band recombination of photogenerated electron-hole pairs, Stutzmann et al (1985) expressed the rate of the dangling bond density change with light exposure time by

$$\frac{dN_s}{dt} \propto np \propto \frac{G^2}{N_s^2} \quad (4.6)$$

In eq. (4.6), the generation rate of the new dangling bond density should be proportional to the product  $np$  of the respective concentrations of electrons and holes because the probability of the dangling bond creation is proportional to both the numbers of electrons and holes. The rate of generation of new dangling bonds,  $dN_s/dt$ , therefore, decreases with the square of the density of the dangling bonds. In this case, the Staebler-Wronski effect is self-limiting since the creation of new dangling bonds is inhibited by the density of stretched weak Si:Si bonds, which are the predecessor of new dangling bonds. As dangling bonds are formed, fewer weak Si:Si bonds are available. Thus, the more dangling bonds there are, the slower new ones are created.

Also, Stutzmann et al (1985) proposed a first-order thermal recovery reaction with a distribution of activation energies between 0.9 and 1.3 eV. The rate equation which they proposed combines both degradation and recovery together with the temperature dependence is expressed by

$$\frac{dN_s}{dt} = K_d \frac{G^2}{N_s^2} - \exp\left(\frac{-E_{dr}}{kT}\right) [N_s - N_s(0)] \quad (4.7)$$

where  $K_d$  is the proportionality coefficient for degradation whose temperature dependence is sufficiently weak to make it approximately constant;  $E_{ar}$  is the activation energy for the recovery;  $N_s(0)$  is the dangling bond density before exposure.

Lee et al (1985) also investigated the recovery kinetics by ESR techniques, but they concluded that recovery can be described by a second-order kinetic model with a single activation energy. According to their model, the recovery rate equation is

$$\frac{dN_s}{dt} = -k_r \exp\left(\frac{-E_{ar}}{kT}\right) N_s^2 \quad (4.8)$$

where  $k_r$  is the proportionality coefficient for recovery;  $E_{ar}$  is the recovery activation energy at 1.1 eV. However, Smith and Wagner (1985) showed that both the Lee and the Stutzmann models could fit experimental results if proper coefficients were chosen.

Eser (1986) also assumed that the degradation process is the result of the breaking of stretched Si:Si bonds. From his experimental work, the light-induced degradation and recovery of defects in *a*-Si:H appear to be thermally activated with single activation energies of 0.1 eV and 1.35 eV, respectively.

Eser's result on recovery was quite different from the previous two models. According to his analysis, the thermal recovery process is a fifth-order reaction of the dangling bond density. He pointed out, however, that his result came from the curve fitting of the experimental result and may not be directly related to the physical processes taking place in the reaction. He concluded that the recovery reaction can only be a second-order process since two coincident and adjacent dangling bonds are required to reestablish stretched Si:Si bonds.

From the models reviewed above, both light-induced degradation and thermal recovery can be described by the reactions activated by single activation energies

which are inversely or directly proportional to the dangling bond density. Also, the rate of thermal recovery should be proportional to the density of the recoverable dangling bonds,  $N_s - N_s(0)$ , however, the reaction order is still controversial. Therefore, the recovery reaction order,  $m$ , will be determined from the experimental data. The recovery rate equation in this study was expressed as

$$\frac{dN_s}{dt} = -k_r \exp\left(\frac{-E_{ar}}{kT}\right) [N_s - N_s(0)]^m \quad (4.9)$$

By combining the recovery model in eq. (4.9) and Stutzmann's degradation model, and replacing the  $K_d$  of the Stutzmann model with a Boltzmann distribution term incorporating the degradation activation energy, the rate equation in this study was expressed as

$$\frac{dN_s}{dt} = k_d \exp\left(\frac{-E_{ad}}{kT}\right) \frac{G^2}{N_s^2} - k_r \exp\left(\frac{-E_{ar}}{kT}\right) [N_s - N_s(0)]^m \quad (4.10)$$

where  $k_d$  is the proportionality coefficient for degradation;  $k_r$  is the proportionality coefficient for recovery;  $E_{ad}$  is the activation energy for the degradation;  $E_{ar}$  is the activation energy for the recovery.

Equation (4.10) is used in the experimental work, both in the numerical form of the differential equation and in the integrated form. To evaluate the dangling bond density in time, we can use eq. (4.10), which can be solved numerically using Euler's forward difference formula.

$$\frac{N_{s,i+1} - N_{s,i}}{\Delta t} = k_d \exp\left(\frac{-E_{ad}}{kT}\right) \frac{G^2}{N_{s,i}^2} - k_r \exp\left(\frac{-E_{ar}}{kT}\right) [N_{s,i} - N_s(0)]^m \quad (4.11)$$

The formula is simple and explicit. Therefore, if  $N_{s,i}$  is known,  $N_{s,i+1}$  can directly be calculated. The accuracy of results and the speed of computation are crucial in numerical methods. One means of reducing the error is to make the step size,

$\Delta t$ , smaller. However, it may result in an increase in both computational time and roundoff error (Ferziger 1981). Therefore, selecting an optimal step size is essential. Table 4.2 shows the simulation results for an hour period by eq. (4.11) with different time steps and arbitrary values of system parameters for comparison.

Table 4.2 Step-Size vs Accuracy

Step size, sec	Final Values	Error
0.1	1.000000	
0.5	1.000030	0.003%
1.0	1.000075	0.007%
5.0	1.000425	0.043%
10.0	1.000858	0.086%
30.0	1.002618	0.262%
60.0	1.005340	0.534%
300.0	1.031658	3.166%

Ten seconds was chosen as the time step in this study as the best compromise between accuracy and computational time. Equation (4.11) can be solved numerically if the activation energies,  $E_{ad}$  and  $E_{ar}$ , the proportionality coefficients,  $k_d$  and  $k_r$ , the recovery reaction order,  $m$ , and the carrier generation rate,  $G$ , are known. We call them the fundamental rate controlling parameters of the samples. The fundamental rate controlling parameters are important variables in evaluating the relative effects of degradation and recovery processes in our analysis and can be evaluated by a combination of experimental and numerical methods.

The change of  $N_s$  in time can be predicted by solving eq.(4.11). The change in carrier lifetime then can be predicted by correlating the change of  $N_s$  by eq.(4.3). The analysis of degradation and recovery to this point has been in terms of the dangling bond density and the carrier lifetime. The quantities which

can be measured experimentally, however, are the short-circuit current, the open-circuit voltage, and the fill factor, using the experimental facilities available for this study. In the next section, a means to correlate a dangling bond density to experimentally measurable quantities will be presented. The carrier lifetime must be a crucial factor for correlating them since the SWE is directly related to the change in carrier lifetime.

### **4.3 Analysis and Modeling of *a-Si:H* Solar Cell Performance**

In the following, we will derive the relationships needed to determine experimentally the fundamental rate controlling parameters which will be used in the performance prediction model.

In Section 4.1, it was cited from prior work that the fill factor is the principal variable changed by degradation. However, no theoretical performance model has been proposed yet which uses a correlation between the fill factor and the carrier lifetime. On the other hand, the change in the short-circuit current is directly related to the change in carrier lifetime. Since prior work has shown that the degradation of  $I_{sc}$  is much more significant than that of  $V_{oc}$ , the degradation of  $I_{sc}$  will be used in the quantitative experimental determination of the fundamental rate controlling parameters in this study.

To correlate  $N_s$  with  $I_{sc}$ , we begin with the current model in terms of the carrier lifetime at low light intensities proposed by Crandall (1982).

$$I = A_c q G l_c \left[ 1 - \exp\left(\frac{-d}{l_c}\right) \right] \quad (4.12)$$

where  $I$  is the current;  $A_c$  is the cell area;  $G$  is the carrier generation rate;  $q$  is the electron charge;  $d$  is the *i*-layer thickness;  $l_c$  is the carrier collection length. The

carrier collection length is defined by

$$l_c = \overline{\mu\tau} E \quad (4.13)$$

where  $E$  is the electric field in the  $i$  layer. If a uniform field in the  $i$  layer is assumed (Crandall 1983), eq. (4.13) can be expressed as

$$l_c = \overline{\mu\tau} (V_a + V_{bi})/d \quad (4.14)$$

where  $V_a$  is the applied voltage;  $V_{bi}$  is the built-in voltage which is approximately the same as the open-circuit voltage (Faughnan and Crandall 1984). Under the short-circuit conditions, the applied voltage,  $V_a$ , due to light is zero and the corresponding carrier collection length,  $l_{co}$ , can be given by

$$l_{co} = \frac{\overline{\mu\tau} V_{bi}}{d} \approx \frac{\overline{\mu\tau} V_{oc}}{d} \quad (4.15)$$

Combining eq. (4.15) and eq. (4.12), the short-circuit current was expressed in this study by the following equation:

$$I_{sc} = \frac{A_c q G \overline{\mu\tau} V_{oc}}{d} \left[ 1 - \exp\left(\frac{-d^2}{\overline{\mu\tau} V_{oc}}\right) \right] \quad (4.16)$$

The initial short-circuit current before the degradation,  $I_{sc}(0)$ , then can be related to the initial carrier lifetime before light exposure,  $\overline{\tau}_o$ , by

$$I_{sc}(0) = \frac{A_c q G \overline{\mu\tau}_o V_{oc}}{d} \left[ 1 - \exp\left(\frac{-d^2}{\overline{\mu\tau}_o V_{oc}}\right) \right] \quad (4.17)$$

From the ratio of the initial  $I_{sc}(0)$  to the  $I_{sc}(t)$  after light exposure, the change in carrier lifetime in this study can be determined from the following equation:

$$\frac{I_{sc}(t)}{I_{sc}(0)} = \frac{\overline{\mu\tau}_t \left[ 1 - \exp\left(\frac{-d^2}{\overline{\mu\tau}_t V_{oc}}\right) \right]}{\overline{\mu\tau}_o \left[ 1 - \exp\left(\frac{-d^2}{\overline{\mu\tau}_o V_{oc}}\right) \right]} \quad (4.18)$$

Therefore, eq. (4.18) is the key to the prediction of the change in carrier lifetime from a directly measured quantity, the  $I_{sc}$ . The change in carrier lifetime then can be directly related to the change in dangling bond density through eq. (4.3). Thus by measuring  $I_{sc}$  while degradation and recovery are occurring, we can determine changes in  $\bar{\tau}$  and  $N_s$  as a function of time. This allows the activation energies and coefficients of proportionality of these processes to be experimentally determined and used in the predictive computer model developed in this study.

To derive the additional basic correlations in the performance prediction model, the correlation between the carrier lifetime and the  $I$ - $V$  characteristics of  $a$ - $Si:H$  proposed by Faughnan and Crandall (1984) is the starting point. They used the Hecht formula (Hecht 1932) to describe the  $I$ - $V$  characteristics of an  $a$ - $Si:H$   $p$ - $i$ - $n$  solar cell:

$$f = \frac{l_c}{d} \left[ 1 - \exp\left(\frac{-d}{l_c}\right) \right] \quad (4.19)$$

where  $f$  is the carrier collection ratio and is defined by

$$f \equiv \frac{\text{electron-hole pairs collected in the external circuit}}{\text{number of photo-generated electron-hole pairs}} \quad (4.20)$$

At the short-circuit condition, the carrier collection ratio,  $f_{sc}$ , is the ratio of the short-circuit current to the light generated current,  $I_L$ , by the definition, and it can be expressed as

$$f_{sc} = \frac{I_{sc}}{I_L} = \frac{l_{co}}{d} \left[ 1 - \exp\left(\frac{-d}{l_{co}}\right) \right] \quad (4.21)$$

By substituting eq. (4.15) into eq. (4.21),  $f_{sc}$  can be expressed as

$$f_{sc} = \frac{\bar{\mu}\bar{\tau}V_{oc}}{d^2} \left[ 1 - \exp\left(\frac{-d^2}{\bar{\mu}\bar{\tau}V_{oc}}\right) \right] \quad (4.22)$$

Then, the ratio of the initial carrier collection ratio,  $f_{sc}(0)$ , to the carrier collection ratio after the degradation due to light exposure occurs,  $f_{sc}(t)$ , for short-circuit conditions can be expressed as

$$\frac{f_{sc}(t)}{f_{sc}(0)} = \frac{\overline{\mu\tau}_t \left[ 1 - \exp\left(\frac{-d^2}{\overline{\mu\tau}_t V_{oc}}\right) \right]}{\overline{\mu\tau}_o \left[ 1 - \exp\left(\frac{-d^2}{\overline{\mu\tau}_o V_{oc}}\right) \right]} \quad (4.23)$$

In this study, it was noted that eq. (4.23) and eq. (4.18) are identical. Therefore, the ratio of the degradation of the carrier collection ratio at the short-circuit condition is identical to the ratio of the degradation of the short-circuit current. From eq. (4.21),  $f_{sc}$  was calculated with different values of  $l_{co}$ . The  $i$ -layer thickness of the sample,  $d$ , is  $0.35 \mu m$  (Willet 1989).

Table 4.3  $l_{co}/d$  vs  $f_{sc}$

$l_{co}/d$	$f_{sc}$	Remarks
1	0.632	samples
10	0.952	
14	0.965	
20	0.975	
30	0.984	

From Table 4.3, it was found that  $f_{sc}$  of the samples has the value of almost unity. Therefore, the short-circuit current is approximately the same as the light generated current, which provides a reasonable basis for the assumption made in Chapter 3 ( $I_{sc} \approx I_L$ ).

We will now introduce the fill factor into our analysis. As mentioned earlier, the major effect of the degradation process is the reduction of the carrier lifetime. This decreases the fill factor, which decreases the output power and current flow.

Similarly, the collection length,  $l_c$ , which is a function of a carrier lifetime, influences the efficiency of an amorphous silicon solar cell through its effect on the fill factor. Smith et al (1985) have presented an empirical relationship between the carrier lifetime and the fill factor by means of the collection length using the data of Faughnan and Crandall (1984).

$$FF = 0.39 + 0.3 \times \log_{10} \left( \frac{l_{co}}{d} \right) = 0.39 + 0.3 \times \log_{10} \left( \frac{\overline{\mu\tau} V_{oc}}{d^2} \right) \quad (4.24)$$

This relationship is the only one proposed for the correlation of the degradation of the carrier lifetime and the degradation of the fill factor and is fully accepted by the photovoltaic module manufacturer. The ratio of the initial fill factor,  $FF(0)$ , to the fill factor after light exposure,  $FF(t)$ , then can be found by

$$\frac{FF(t)}{FF(0)} = \frac{0.39 + 0.3 \times \log_{10} \left( \frac{\overline{\mu\tau}_t V_{oc}}{d^2} \right)}{0.39 + 0.3 \times \log_{10} \left( \frac{\overline{\mu\tau}_o V_{oc}}{d^2} \right)} \quad (4.25)$$

The characteristics of cells, however, may vary from sample to sample according to unavoidable slight differences in sample preparation. Therefore, the empirical relationship in eq. (4.25) may not be generally acceptable for predicting the performance of different cells. From eq. (4.25), it is reasonable to assume that the degradation in fill factor can be expressed solely as a function of the degradation in carrier lifetime. A similar empirical correlation was experimentally determined for the G4000 sample in this study, which was of the form:

$$\frac{FF(t)}{FF(0)} = C \left( \frac{\overline{\mu\tau}_t}{\overline{\mu\tau}_o} \right)^n \quad (4.26)$$

Equation (4.26) is conceptually identical to eq. (4.25), however, eq. (4.26) does not include the cell thickness term,  $d$ , since the performance characteristics may not be dependent on the thickness as in eq. (4.25). The Smith model was compared and

validated with the experimentally determined model in eq. (4.26). Details of this part of the study will be presented in the next chapter.

We will now combine our degradation and recovery analysis with the photovoltaic conversion efficiency to predict the effect of the degradation and recovery processes. The relation between the photovoltaic cell efficiency with and without degradation ( $\eta_t$  and  $\eta_o$ , respectively) can be expressed by the following functional relationship if light intensity remains the same:

$$\frac{\eta_t}{\eta_o} = \frac{P_m(t)}{P_m(0)} = \frac{FF(t) V_{oc}(t) I_{sc}(t)}{FF(0) V_{oc}(0) I_{sc}(0)} = \frac{FF(t) I_{sc}(t)}{FF(0) I_{sc}(0)} \quad (4.27)$$

In eq. (4.27), the open-circuit voltages,  $V_{oc}(t)$  and  $V_{oc}(0)$ , have cancelled out due to their similar values. From eq. (4.27), the degradation in conversion efficiency can be expressed by multiplication of the degradation in the fill factor and the degradation in the short-circuit current. Thus the equations that predict the degradation of the array performance have been developed using the experimentally determined coefficients and activation energies. The value of  $N_s$  as a function of time can be determined from this value, the degraded value of  $\bar{\mu\tau}$  and then the degraded fill factor can be calculated. Finally, the degraded overall efficiency can be calculated.

The long-term performance model which has been developed in this study depends on the calculation of the fill factor and the short-circuit current with and without degradation to determine the photovoltaic array efficiency. The performance of amorphous solar cells then can be predicted by combining the following two analyses:

1. Photovoltaic power generation without considering the degradation effect discussed in Chapter 3.
2. Photovoltaic conversion efficiency decay due to the degradation discussed in this chapter.

From the above two analyses, the electric power generated with the degradation effect,  $P_{deg}$ , can be calculated by combining eq. (3.24) and eq. (4.27).

$$P_{deg} = P_m \times \frac{\eta_t}{\eta_o} \quad (4.28)$$

In this section, the change in carrier lifetime due to the SWE was correlated to the change in the short-circuit current, which is an experimentally measurable quantity. The degradation in the fill factor can also be correlated to the change in carrier lifetime by an experimentally determined correlation in eq. (4.26). The experimental procedures will be presented in the next chapter.

## CHAPTER 5

### EXPERIMENTAL METHODOLOGY AND RESULTS

The goal of the experimental part of this study is the determination of the fundamental parameters that determine the relative rates of degradation and recovery of the samples. These parameters were evaluated from the change in the experimentally measured values of  $I_{sc}$ , using the correlation developed in Chapter 4.

Before performing the experiments regarding the degradation and annealing processes, the carrier generation rate,  $G$ , was determined since the rate of degradation depends partly on the value of  $G$ . During each degradation experiment,  $G$  must be constant. Since this condition is not easily fulfilled in natural sunlight, an artificial lamp which yields a constant light intensity was used in the experiment. Unfortunately, the spectral distribution of light produced by the artificial lamp is different from that of sunlight. Thus we need a method of calculating the  $G$  value for the artificial lamp from the accepted  $G$  value of natural sunlight.

#### 5.1 Determination of $G$ for Artificial Lamp

The value of  $G$  from any light source is a function of the light intensity and the spectral distribution of the incident light. Thus the carrier generation rate under natural sunlight,  $G_{sun}$ , is a function of the sun's location in the sky, since the incident insolation intensity and spectral distribution change as a function of the sun's location. The most important parameter which determines the light intensity

and the spectral distribution of sunlight is the length of the light path through the atmosphere. The length of the light path is embodied in the air mass concept, where the air mass (AM) is unity when the sun is directly overhead, and is zero above the earth's atmosphere.

The accepted value of the carrier generation rate for *a-Si:H*,  $G_{std}$ , in sunlight at  $1000 \text{ W/m}^2$  under AM1.5 is  $1.6 \times 10^{21} \text{ cm}^{-3} \text{ sec}^{-1}$  (Smith et al. 1985; Ichikawa et al. 1987). This value of  $G$  is only correct for the spectral distribution of sunlight at AM1.5. The solar spectral distribution at various air mass values and the spectral response of *a-Si:H* are shown in Fig. 5.1 and Fig. 5.2, respectively.

The carrier generation rate of the light source used in the experimental part of this study is not directly measurable. However, the short-circuit current of a test cell is a directly measurable quantity, which is directly proportional to  $G$ , which in turn a function of the spectral distribution of the incident light, the spectral response of *a-Si:H*, and the light intensity under short-circuit conditions.

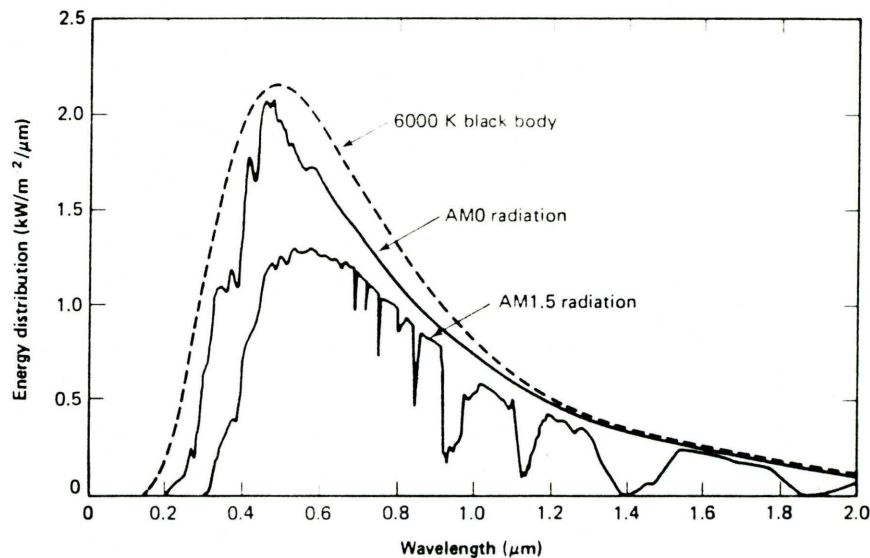


Fig. 5.1 Solar Spectral Distribution vs Air Mass

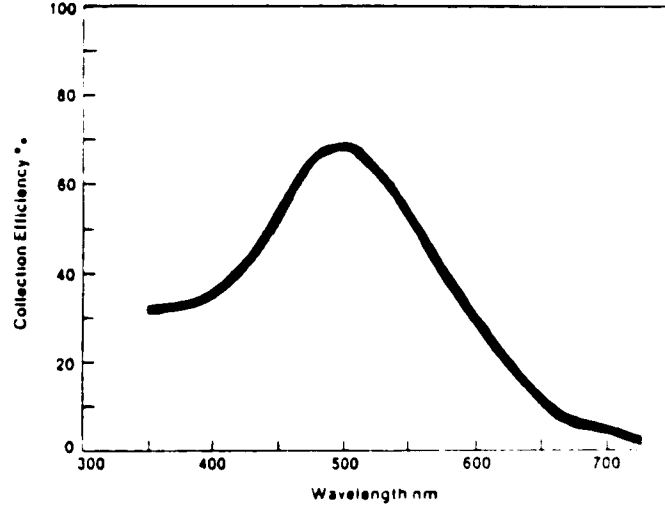


Fig. 5.2 Spectral Collection Efficiency of *a-Si:H*

If the spectral distribution of sunlight is constant and the intensity varies, the carrier generation rate at measured sunlight intensity,  $G_{sun}$ , then can be related to the standard values by

$$G_{sun} = \frac{I_{sun}}{I_{std,sun}} \times G_{std,sun} \quad (5.1)$$

where  $I_{sun}$  is a measured sunlight intensity and  $I_{std,sun}$  is the standard solar intensity of  $1000 \text{ W/m}^2$  used when  $G_{std,sun}$  was evaluated.

If the intensity of light from a lamp and from the sun is the same, but their spectral distributions vary, their carrier generation rates and short-circuit currents can be related by

$$G_{lamp} = \frac{I_{sc,lamp}}{I_{sc,sun}} \times G_{sun} \quad (5.2)$$

where  $I_{sc,lamp}$  and  $I_{sc,sun}$  are the measured short-circuit currents under artificial light and sunlight, respectively. By combining eq. (5.1) and eq. (5.2),  $G_{lamp}$  can be expressed as

$$G_{lamp} = \frac{I_{sc,lamp}/I_{std,sun}}{I_{sc,sun}/I_{sun}} \times G_{std,sun} \quad (5.3)$$

The short-circuit currents produced by  $1000 \text{ W/m}^2$  sunlight (at an AM of 1.5) and by the same intensity of artificial light were measured in order to find  $G_{lamp}$  for that light intensity from eq. (5.3). The total light intensities were measured with an Eppley PSP pyranometer, since it is insensitive to the wavelength of insolation. Halogen projector lamps ELH (120V-300W) were used as the test lamp. Table 5.1 shows the short-circuit currents measured under sunlight and the test lamp for the samples used in the experiment.

Table 5.1 Measured Short-Circuit Currents

Samples	Sunlight $\text{W/m}^2$	$I_{sc,sun}$ $\text{mA}$	Lamp $\text{W/m}^2$	$I_{sc,lamp}$ $\text{mA}$
A	1024	30.02	1000	26.18
B	1105	30.91	1000	26.64
C	1033	29.63	1000	26.16
D	1042	30.07	1000	27.02
average	1051	30.16	1000	26.50

Table 5.2 was prepared to correlate  $G_{lamp}$  and  $G_{std,sun}$  by eq. (5.3). From Table 5.2, it was found that the spectral characteristics of the halogen projector lamps are fairly close to those of sunlight. The variation of  $I_{sc}/I_{light}$  may come from slight differences in sample characteristics. From eq. (5.3), the carrier generation rate of the halogen lamps at  $1000 \text{ W/m}^2$ ,  $G_{lamp}$  was expressed by the following equation in this study:

Table 5.2  $I_{sc}$  divided by Light Intensity

Samples	#1 $I_{sc,sun}/I_{sun}$ $mA\cdot m^2/W$	#2 $I_{sc,lamp}/I_{lamp}$ $mA\cdot m^2/W$	#2/#1
A	0.02932	0.02618	89.30%
B	0.02797	0.02664	95.24%
C	0.02868	0.02616	91.20%
D	0.02886	0.02702	93.63%
average	0.02871	0.02650	92.34%

$$G_{lamp} = 0.92 \times G_{std,sun} \quad (5.4)$$

The values of the parameters which have now been determined for the G4000 samples are:

- Initial dangling bond density,  $N_s(0)$ :  $5 \times 10^{15} cm^{-3}$
- Initial carrier lifetime-mobility product,  $\bar{\mu}\tau_o$ :  $2.0 \times 10^{-8} cm^2 V^{-1}$ .
- Built-in voltage,  $V_{bi}$ : 0.857 V
- Intrinsic *i*-layer thickness,  $d$ : 0.35  $\mu m$
- Carrier generation rate,  $G_{lamp}$ :  $0.92 \times 1.6 \times 10^{21} cm^{-3} sec^{-1}$

These parameters will be used to solve eq. (4.11) and to correlate the dangling bond density and measured quantities. In the next section, the experimental methodology and the analytical procedure for the determination of the fundamental rate controlling parameters will be presented.

## **5.2 Experimental Methodology**

To experimentally determine the fundamental parameters which determine the rates of degradation and recovery, controlled conditions which eliminate either

degradation or recovery are imposed on the sample. At low temperatures, the recovery effect will be negligible. Also, light-induced degradation is obviously impossible in the dark. Thus, using controlled conditions, either of the two effects can be prevented, which allows the activation energy and the proportionality coefficient of the other effect to be evaluated. During light exposure at normal array operating temperatures, however, degradation and recovery processes occur simultaneously.

Based on the phenomena mentioned above, the following experiments were performed to determine the fundamental rate controlling parameters:

1. Degradation at a constant  $50^{\circ}F$  with light intensities of  $1000 W/m^2$  and  $2000 W/m^2$ .
2. Annealing and recovery at several temperatures ( $170^{\circ}F$ ,  $235^{\circ}F$ ,  $270^{\circ}F$ ,  $300^{\circ}F$ , and  $340^{\circ}F$ ) in the dark.
3. Degradation at a light intensity of  $1000 W/m^2$  without temperature control. The purpose of this experiment was to determine if degradation is decreased at normal array operating temperatures by a simultaneous recovery process.

The G4000 samples were provided by the ARCO Solar Inc. for the experiment. During the experiment, halogen projector lamps ELH (120V-300W) were used. The slight variation of light intensity at a measuring point due to voltage fluctuation was monitored by using a Li-Cor Pyranometer (Model PY-7130), which was calibrated with the Eppley PSP pyranometer. The annealing was carried out using the electric heater (Model HP-A1915B). Figure 5.3 shows the experimental apparatus for the measurement.

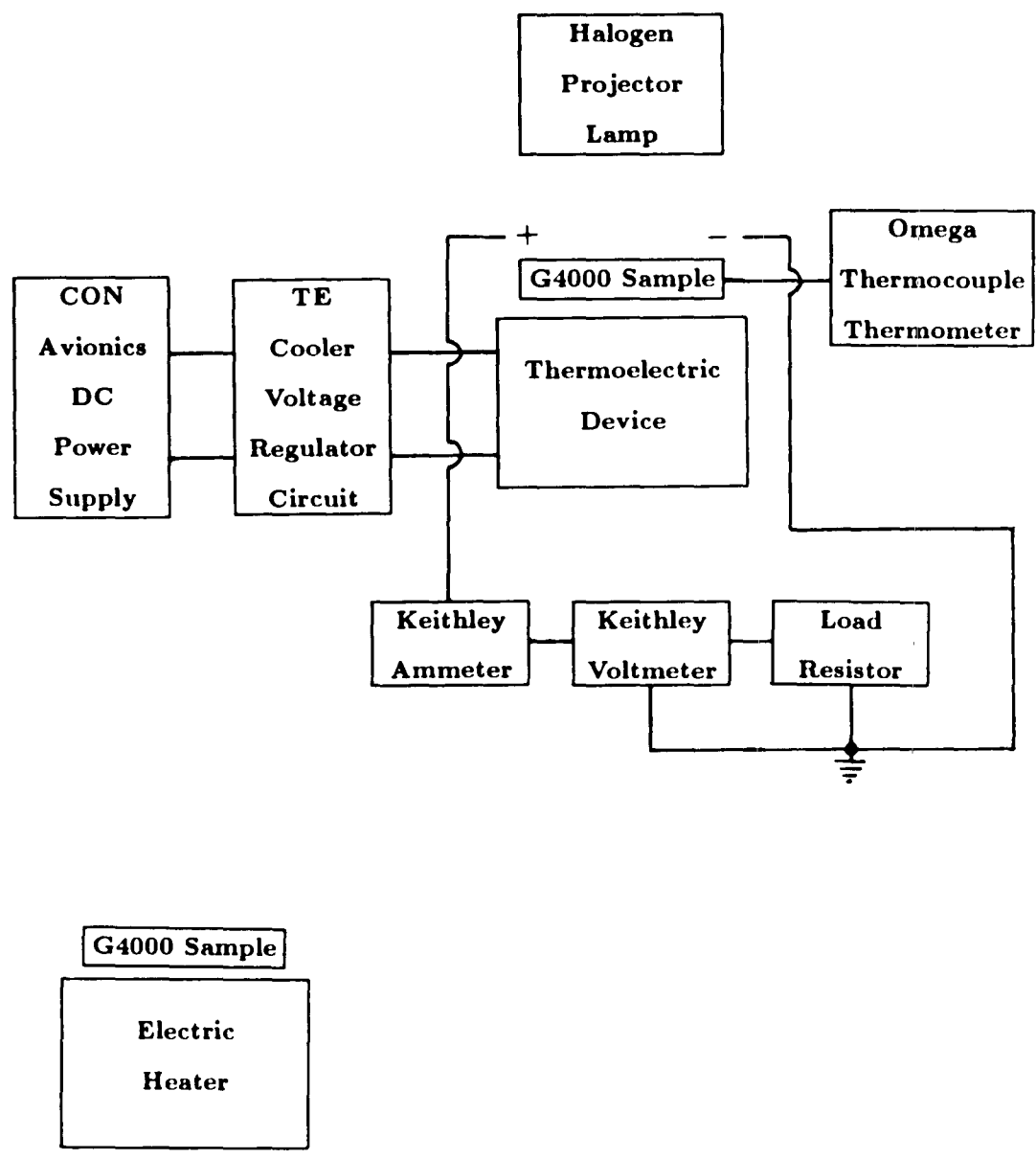


Fig. 5.3 Experimental Apparatus

The G4000 samples were at the as-grown state before the experiment. The experiment for light-induced degradation was performed first for 96 hours. Then, the degraded samples were annealed at different temperatures. The percent degradation in the short-circuit current,  $PDI_{sc}$ , and the percent recovery in the short-circuit current,  $PRI_{sc}$ , were expressed by the following equations in this study:

$$PDI_{sc} (\%) = \frac{I_{sc}(0) - I_{sc}(t)}{I_{sc}(0)} \times 100 \quad (5.5)$$

$$PRI_{sc} (\%) = \frac{I_{sc}(t) - I_{sc,deg}}{I_{sc}(0) - I_{sc,deg}} \times 100 \quad (5.6)$$

where  $I_{sc,deg}$  is the short-circuit current at the beginning of annealing.

By annealing, the degraded samples were returned to a state which is close to the as-grown state, but not to the same state. Also, the samples never recovered to a state better than the as-grown state. From the experimental data and the simulation study using the numerical model in eq. (4.11), it was also found that the percent recovery in the short-circuit current,  $PRI_{sc}$ , was virtually independent of the short-circuit current value at the initiation of the annealing process,  $I_{sc,deg}$ . For example, if sample-A is more degraded than sample-B, the value  $I_{sc}(0) - I_{sc,deg}$  of sample-A is greater than that of sample-B. However, the value  $I_{sc}(t) - I_{sc,deg}$  of sample-A is also greater than that of sample-B. From the experiment, the ratio,  $PRI_{sc}$ , was found to be fairly constant. That means the percent recovery does not depend on the absolute value of initial degraded state prior to annealing. This is an important point regarding the determination of the fundamental rate controlling parameters in this study.

Due to the point mentioned above, the recovery parameters,  $m$ ,  $E_{ar}$ , and  $k_r$ , were calculated from the experimental data first. Then, possible sets of the

degradation parameters,  $E_{ad}$  and  $k_d$ , were determined from degradation data obtained at two light intensities ( $1000 \text{ W/m}^2$  and  $2000 \text{ W/m}^2$ ) and at the specified low temperature, where recovery processes are negligible. Finally, using data from experiments where degradation and recovery occur simultaneously and the best set of  $E_{ar}$ ,  $k_r$ , and  $m$  determined previously, the best coincident set of  $E_{ad}$  and  $k_d$  was chosen.

The best sets of the fundamental rate controlling parameters for the samples were determined by evaluating the root mean square errors ( $RMSE$ ), which can be expressed as

$$RMSE = \sqrt{\frac{\sum RE_i^2}{\sum N_i}} \quad (5.7)$$

where  $N_i$  is the number of measurement;  $RE$  is the relative error and is given by

$$RE = \frac{\text{experimental} - \text{simulated}}{\text{experimental}} \quad (5.8)$$

Even though degradation preceded recovery in the experimental procedure, the annealing process and the calculation of the recovery parameters,  $m$ ,  $E_{ar}$ , and  $k_r$  will be discussed first.

### 5.3 Determination of $m$ , $E_{ar}$ , and $k_r$

The experiment for the determination of  $m$ ,  $E_{ar}$ , and  $k_r$  was carried out as follows:

1. Maintain the degraded sample at high temperatures ( $170^\circ \text{ F}$ ,  $235^\circ \text{ F}$ ,  $270^\circ \text{ F}$ ,  $300^\circ \text{ F}$ , and  $340^\circ \text{ F}$ ) in the dark to prevent the light-induced degradation. The high temperatures were maintained by using an electric heater. The

sample temperatures were monitored using an Omega Thermocouple Thermometer (Model 660).

2. Measure the initial value of  $I_{sc}$  before annealing.
3. Perform the experiment for several hours in the dark.
4. Measure the values of  $I_{sc}$  at 1 - 2 hour intervals, using the same light intensity as in step-2.
5. Table 5.3 shows the experimental results of annealing as a function of temperature and graphically in Fig. 5.4

Table 5.3 Recovery in Short-Circuit Currents

Samples	Annealing temperature, °F	$I_{sc}$ mA	% Recovery of $I_{sc}$	Elapsed time hours
P	300	24.58	76.92%	initial
		26.08		2
		26.53		as-grown
A	270	24.61	60.51%	initial
		25.56	79.62%	2
		25.86	80.89%	4
		25.88		6
		26.18		as-grown
B	300	25.16	47.47%	initial
		26.19	82.49%	1
		26.95	83.87%	2
		26.98	85.71%	3
		27.02		6
	27.33		as-grown	
C	300	25.25	53.67%	initial
		26.20	81.92%	1
		26.70	84.18%	2
		26.74	86.44%	3
		26.78		6
	27.02		as-grown	

D	340	24.75	83.60%	initial
		26.33		1
		26.54		2
		26.57		3
		26.64		as-grown
E	170	15.39	25.81%	initial
		15.47		10
		15.53		20
		15.59		35
		15.70		as-grown
F	235	15.50	38.89%	initial
		15.85		2
		16.09		4
		16.20		6
		16.40		as-grown
G	170	15.70	32.04%	initial
		16.03		10
		16.15		20
		16.23		35
		16.73		as-grown

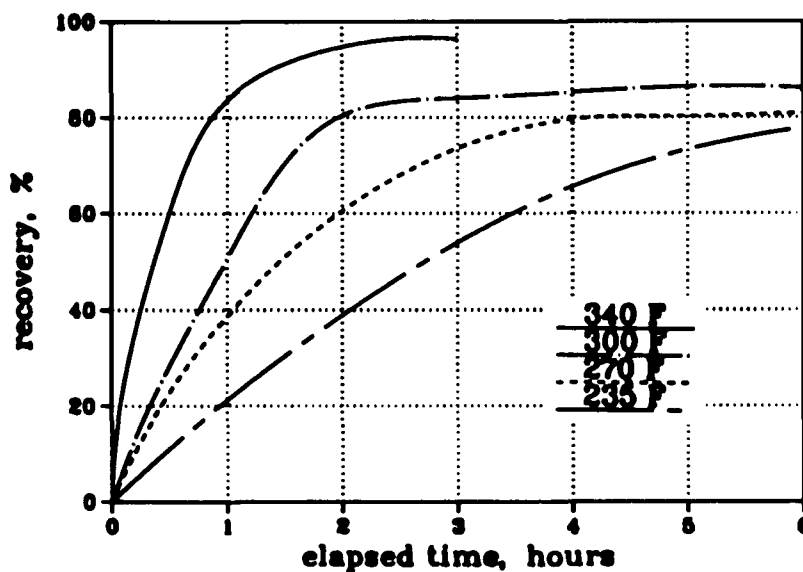


Fig. 5.4 Percent Recovery vs Temperature

The rates of recovery of the short-circuit currents of the samples appeared to follow a similar pattern, where the initial recovery rate is rapid, and then asymptotically approaches the as-grown state. The three annealing tests at  $300^{\circ}F$  are tabulated in Table 5.4 and graphically in Fig. 5.5. From Table 5.4, it can be seen that the percent recovery after a given time interval is approximately the same for the three cases even though their initial degraded states and as-grown states were different.

Table 5.4 Average Values for Percent Recovery in  $I_{sc}$   
at  $300^{\circ}F$  Annealing

Elapsed time <i>hours</i>	Sample P	Sample B	Sample C	Average values
1		47.47%	53.67%	50.57%
2	76.92%	82.49%	81.92%	80.44%
3		83.87%	84.18%	84.03%
6		85.71%	86.44%	86.08%

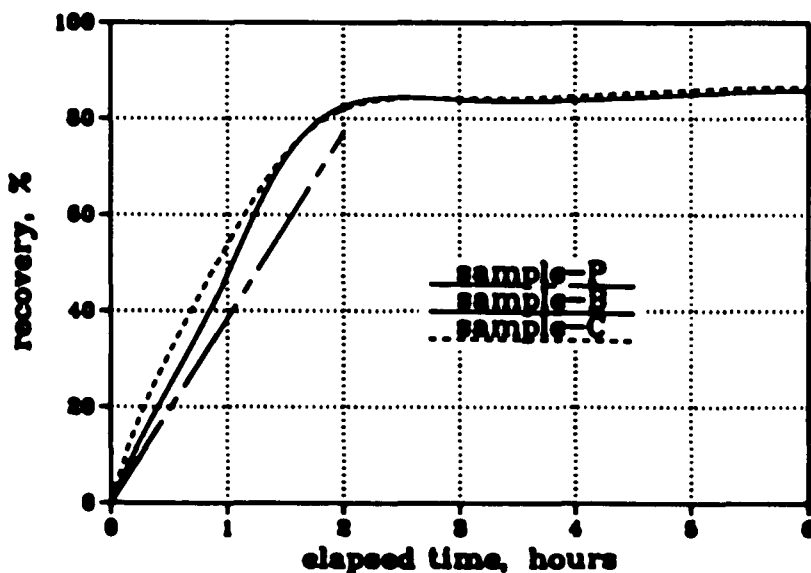


Fig. 5.5 Percent Recovery at  $300^{\circ}F$

6. Solve eq. (4.11) with different values of  $E_{ar}$  and  $k_r$  for  $N_s(t)$ . Since the experiments were conducted in the dark,  $G = 0$  and the degradation term is zero. Then calculate  $PRI_{sc}$  using  $N_s(t)$ . Also calculate  $PRI_{sc}$  from the experimental  $I_{sc}(t)$  measurements. The two values of  $PRI_{sc}$  are compared by evaluating their  $RMSE$ . Tables 5.5 and 5.6 show the best sets of  $E_{ar}$  and  $k_r$  for second-order ( $m=2$ ) and first-order ( $m=1$ ) reactions, where  $E_{ar}$  varies from  $0.8 eV$  to  $0.5 eV$ . The best set at each  $E_{ar}$  was determined by evaluating the  $RMSE$  of each set.

Table 5.5  $RMSE$  of the Best Sets of  $E_{ar}$  and  $k_r$   
2nd-order Reaction

$E_{ar}, eV$ $k_r, cm^3 sec^{-1}$	0.8 $2 \times 10^{-10}$	0.7 $1 \times 10^{-11}$	0.6 $5 \times 10^{-13}$	0.5 $2.5 \times 10^{-14}$
300° F	20.79%	14.72%	9.69%	8.39%
340° F	3.08%	2.68%	7.28%	14.23%
270° F	6.02%	3.76%	3.47%	7.71%
235° F	16.45%	14.72%	12.53%	13.35%
170° F	24.91%	7.92%	9.06%	27.02%
average	16.32%	11.16%	9.91%	15.40%

Table 5.6  $RMSE$  of the Best Sets of  $E_{ar}$  and  $k_r$   
1st-order Reaction

$E_{ar}, eV$ $k_r, cm^3 sec^{-1}$	0.8 $1.5 \times 10^6$	0.7 $8 \times 10^4$	0.6 3750	0.5 175
300° F	30.16%	23.18%	12.26%	9.12%
340° F	11.34%	9.42%	3.80%	7.46%
270° F	16.31%	13.78%	9.10%	10.15%
235° F	19.51%	14.98%	17.67%	20.37%
170° F	42.21%	21.28%	9.30%	29.10%
average	26.58%	17.71%	11.43%	18.03%

From Tables 5.5 and 5.6, it can be seen that the second-order reaction ( $m=2$ ) is somewhat better than the first-order model ( $m=1$ ) over a wide range of annealing temperatures (see Fig. 5.6). Since the minima in these two cases were not clearly dissimilar, the possibility of a combination of a first and a second order process was evaluated. The best combination, 35% of first-order and 65% of second-order, resulted in a *RMSE* of 8.95%, which was not a significant improvement. Since the second-order process was the better single process and the complexity of a combined process was not justified by a significant improvement, a second-order process was used to determine  $E_{ar}$  and  $k_r$  in this study.

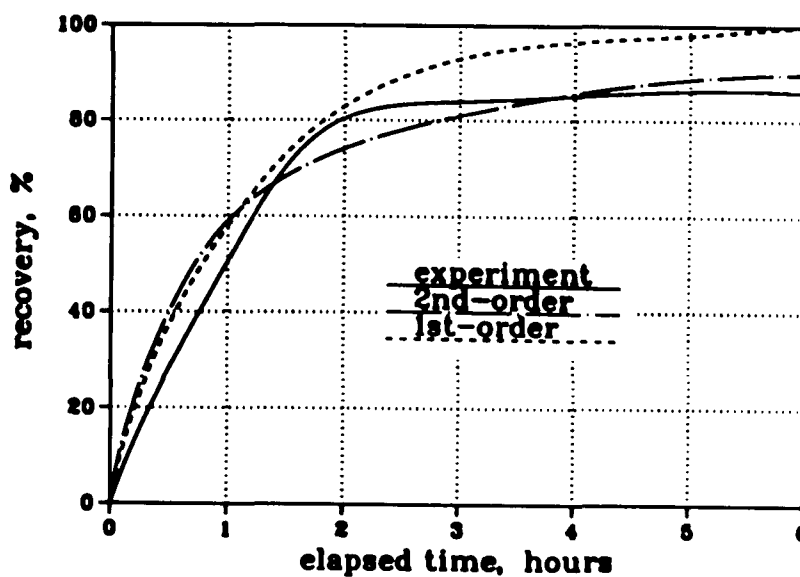


Fig. 5.6 Percent Recovery vs Annealing Reaction Order

From the *RMSE* analysis using the experimental data and the simulation study, the best set of the recovery parameters for the samples is

$$m = 2 \quad E_{ar} = 0.6 \text{ eV} \quad k_r = 5 \times 10^{-13} \text{ cm}^3 \text{ sec}^{-1}$$

7. The parameters obtained above will be used for the determination of the degradation parameters.

#### **5.4 Determination of $E_{ad}$ and $k_d$**

The determination of  $E_{ad}$  and  $k_d$  was carried out as follows:

1. Maintain the test sample temperature at a constant  $50^\circ F$  to make the thermal recovery effect negligible.  $50^\circ F$  was maintained by using a bismuth-telluride Peltier-effect cooling device. The sample temperatures were monitored using an Omega Thermocouple Thermometer (Model 660).
2. Adjust the light intensity to  $1000 W/m^2$  and measure the initial values of  $I_{sc}$ ,  $V_{oc}$ , and  $FF$  immediately after the sample is exposed to the light source. The value of  $G$  for this artificial light intensity was determined by the procedure described previously.
3. From the initial measurement, find the maximum power point. Adjust the load resistor to the maximum power point. This is the optimal load condition for the sample.
4. Measure the values of  $I_{sc}$ ,  $V_{oc}$ , and  $FF$  for every 24 hour period.
5. Adjust the light intensity to  $2000 W/m^2$  and repeat the above procedures. The value of  $G$  for this light intensity was determined by the previously described procedure.
6. Tables 5.7 and 5.8 show the experimental results of the degradation of short-circuit current. The data in Table 5.7 is shown graphically in Fig. 5.7. The average degradation rates for  $1000$  and  $2000 W/m^2$  light intensities are compared in Fig. 5.8.

Table 5.7 Degradation in Short-Circuit Currents  
 $1000 \text{ W/m}^2$  &  $50^\circ \text{F}$

Samples	$I_{sc}$ <i>mA</i>	% Degradation of $I_{sc}$	Elapsed time <i>hours</i>
A	26.18		initial
	25.21	3.71%	24
	24.91	4.85%	48
	24.64	5.88%	72
	24.45	6.61%	96
B	26.64		initial
	25.64	3.75%	24
	25.26	5.18%	48
	24.98	6.23%	72
	24.78	6.98%	96
C	27.02		initial
	26.13	3.29%	24
	25.43	5.88%	48
	25.25	6.55%	72

Table 5.8 Degradation in Short-Circuit Currents  
 $2000 \text{ W/m}^2$  &  $50^\circ \text{F}$

Samples	$I_{sc}$ <i>mA</i>	% Degradation of $I_{sc}$	Elapsed time <i>hours</i>
D	54.52		initial
	50.23	7.87%	24
	49.05	10.03%	48
E	54.32		initial
	50.83	6.42%	24

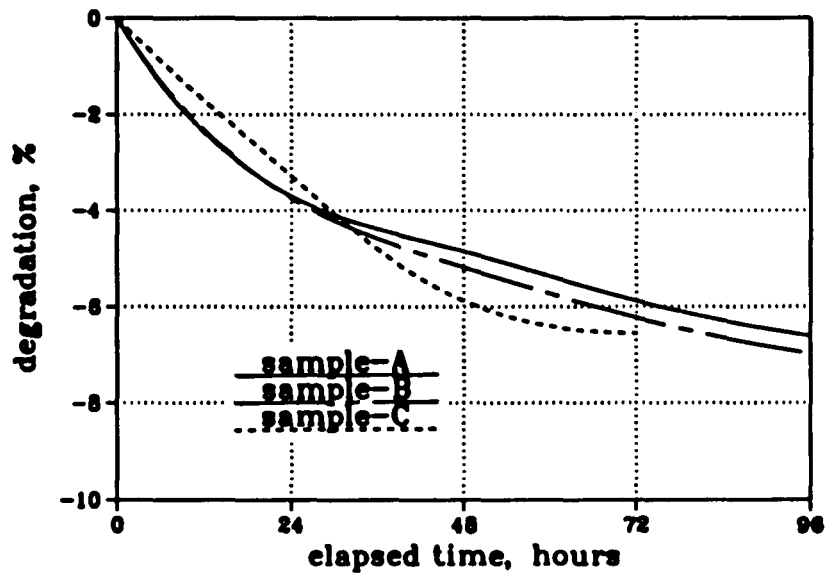


Fig. 5.7 Percent Degradation at  $1000 \text{ W/m}^2$  &  $50^\circ \text{F}$

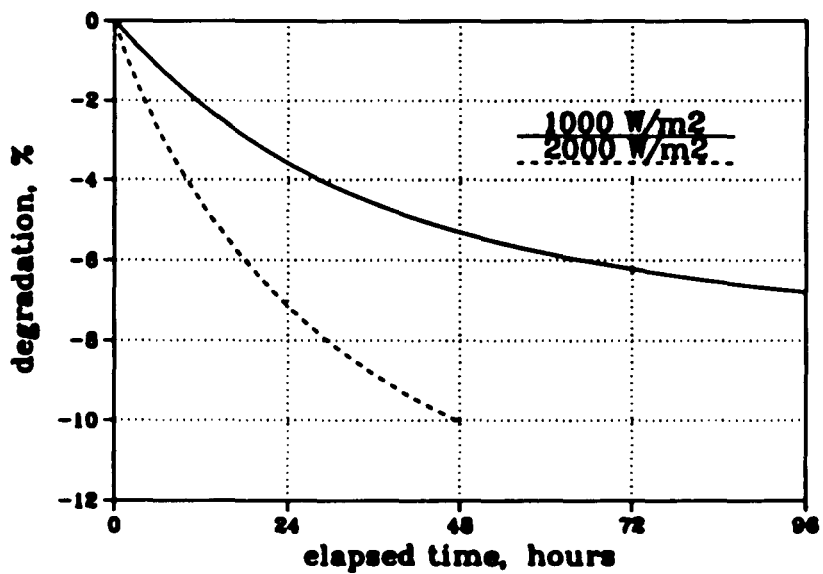


Fig. 5.8 Percent Degradation vs Light Intensity

The rates of degradation of the short-circuit currents of all samples were similar. The degradation rates of the samples exposed to  $2000 \text{ W/m}^2$  were approximately double those of samples exposed to  $1000 \text{ W/m}^2$ . All samples had an initial rapid degradation rate, which decreased with increasing exposure time. The average value of the percent degradation of  $I_{sc}$  after the same elapsed time was used for predicting  $E_{ad}$  and  $k_d$ .

6. Solve eq.(4.11) for  $N_s(t)$  with different values of  $E_{ad}$  and  $k_d$ , using the recovery parameters ( $m$ ,  $E_{ar}$ ,  $k_r$ ) obtained in the annealing process. At  $50^\circ\text{F}$ , the recovery process is virtually negligible. Then calculate  $PDI_{sc}$  using  $N_s(t)$ . Also calculate  $PDI_{sc}$  from  $I_{sc}(t)$  data, and the resultant  $PDI_{sc}$  values were evaluated. Table 5.9 shows the best coincident sets of  $E_{ad}$  and  $k_d$  for  $E_{ad}$  from  $1.0 \text{ eV}$  to  $0.03 \text{ eV}$ . The best coincident set at each  $E_{ad}$  was determined by evaluating the  $RMSE$  of each set.

Table 5.9  $RMSE$  of the Best Coincident Sets of  $E_{ad}$  and  $k_d$

$E_{ad}$ eV	$k_d$ $\text{cm}^{-3} \text{ sec}$	$1000 \text{ W/m}^2$ $50^\circ\text{F}$	$2000 \text{ W/m}^2$ $50^\circ\text{F}$	average
0.10	102	2.78%	2.89%	2.82%
0.09	68	2.84%	2.77%	2.82%
0.08	45	2.76%	2.84%	2.79%
0.07	30	2.89%	2.73%	2.83%
0.06	20	2.96%	2.65%	2.86%
0.05	13	2.64%	3.06%	2.79%
0.04	8	3.63%	2.51%	3.30%
0.03	6	3.86%	2.47%	3.46%

From Table 5.9, it is difficult to determine which coincident set of  $E_{ad}$  and  $k_d$  is the best one for the samples. Thus, the best coincident sets in Table 5.9 were evaluated by similarly calculating  $PDI_{sc}$  from  $N_s(t)$  for the best coincident

sets and comparing these to  $PDI_{sc}$  values calculated from  $I_{sc}(t)$  data from the results of the degradation experiment at an elevated temperature. Table 5.10 shows the experimental results at  $1000 W/m^2$  without temperature control. The sample temperature was increased to  $120^\circ F$  due to incident light intensity and was maintained within  $\pm 5^\circ F$  during the experiment by heat transfer with the environment. Table 5.11 shows the  $RMSE$  analysis. Figure 5.9 shows the reduction in degradation at elevated temperature. Note that degradation is slightly less at the higher temperature.

Table 5.10 Degradation in Short-Circuit Currents  
 $1000 W/m^2$  &  $120^\circ F$

Samples	$I_{sc}$ <i>mA</i>	% Degradation of $I_{sc}$	Elapsed time <i>hours</i>
F	27.12		initial
	26.08	3.83%	24
	25.83	4.76%	48
	25.57	5.72%	72
	25.48	6.05%	96
G	27.32		initial
	26.43	3.26%	24
	25.92	5.12%	48
	25.78	5.64%	72

Table 5.11  $RMSE$  of the Best Coincident Sets of  $E_{ad}$  and  $k_d$   
 $1000 W/m^2$  &  $120^\circ F$

$E_{ad}$	$k_d$	$RMSE$		$E_{ad}$	$k_d$	$RMSE$
0.10	102	20.12%		0.06	20	11.21%
0.09	68	17.92%		0.05	13	7.94%
0.08	45	15.44%		0.04	8	2.59%
0.07	30	13.29%		0.03	6	5.55%

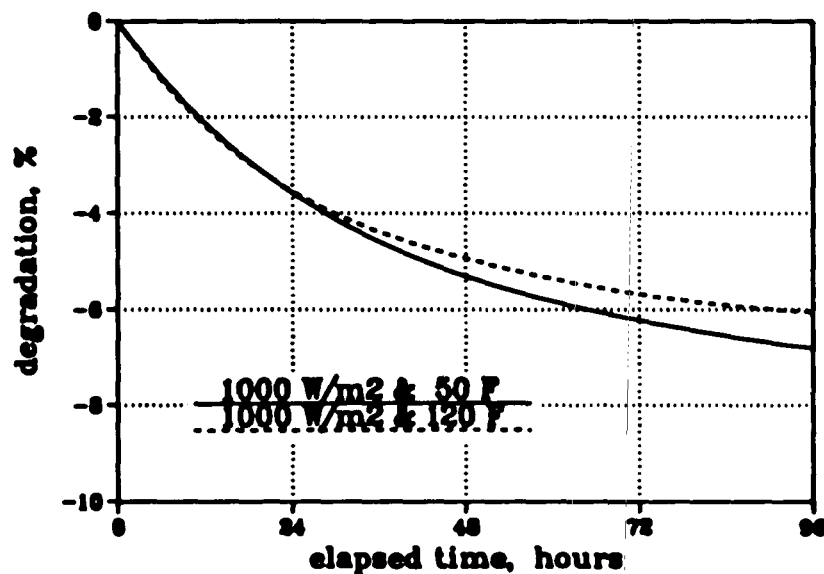


Fig. 5.9 Degradation Effect vs Temperature

From the observation of Table 5.11, the best set of  $E_{ad}$  and  $k_d$  for the samples is

$$E_{ad} = 0.04 \text{ eV} \quad k_d = 8 \text{ cm}^{-3} \text{ sec}$$

All the fundamental rate controlling parameters in eqn (4.11) have now been determined and have the following values in this study:

- Degradation activation energy,  $E_{ad}$ : 0.04 eV
- Recovery activation energy,  $E_{ar}$ : 0.6 eV
- Coefficient for degradation,  $k_d$ :  $8 \text{ cm}^{-3} \text{ sec}$
- Coefficient for recovery,  $k_r$ :  $5 \times 10^{-13} \text{ cm}^3 \text{ sec}^{-1}$
- Recovery reaction order,  $m$ : 2

Equation (4.11) now can be solved in the predictive model with the parameters obtained. The change in the dangling bond density can be predicted and

and correlated to the change in carrier lifetime. The degradation in the fill factor then can be correlated to the change in carrier lifetime by eq. (4.26). This will be discussed in the next section.

### 5.5 Correlation between Fill Factor and $\overline{\mu\tau}$

During the degradation experiment, the degradation in the fill factor was also measured. However, it is not a directly measurable quantity, and is determined by calculating the maximum value of the product of various measured combinations of the load currents and voltages. Table 5.12 shows the ratio of the fill factor after light exposure,  $FF(t)$ , to the initial fill factor,  $FF(0)$ . The degradation ratio in the fill factor followed the same pattern as that of the short-circuit current. Also, since there was no significant difference in the degradation pattern in the fill factor between samples used, the average values of the degradation ratio will be presented.

Table 5.12 Degradation Ratio in Fill Factor

Elapsed time <i>hours</i>	1000 $W/m^2$ 50° $F$	2000 $W/m^2$ 50° $F$	1000 $W/m^2$ 120° $F$
0	100.00%	100.00%	100.00%
24	91.93%	88.28%	92.19%
48	88.69%	85.99%	91.10%
72	86.51%		89.75%
96	86.04%		

The change in  $\overline{\mu\tau}$  was calculated by solving eq. (4.11) with the experimentally determined parameters. The ratio of  $\overline{\mu\tau}_t$  to  $\overline{\mu\tau}_0$  then was calculated and tabulated in Table 5.13.

Table 5.13 Degradation Ratio in  $\overline{\mu\tau}$ 

Elapsed time <i>hours</i>	1000 $W/m^2$ 50° $F$	2000 $W/m^2$ 50° $F$	1000 $W/m^2$ 120° $F$
0	100.00%	100.00%	100.00%
24	50.11%	32.67%	48.07%
48	40.72%	26.21%	40.44%
72	35.95%		37.32%
96	32.90%		

The degradation in the fill factor now can be correlated with the degradation in carrier lifetime using the data in Table 5.12 and Table 5.13. For correlating the two parameters, the Programming Language for the Analysis of Economic Time Series (PLANETS 1984) was used. The PLANETS is a software for the analysis and management of data. As the name implies, the PLANETS was designed primarily for applications involving economic time series data. However, the PLANETS can also be used to analyze and manipulate data, which yields correlation coefficients.

The empirical correlation can be used to predict the degradation ratio in the fill factor for any calculated degradation ratio in carrier lifetime. The value of this prediction is judged by how well the correlation fits the original data. The correlation factor is a measure of the variation of the dependent variable that can be accounted for by the model. The correlation factor varies from 0 to 1 with the values near 1 indicating that the equation can be used as a predictor with little risk of error. By running the PLANETS with the experimental data, the correlation factor was very satisfactory, having a value of 0.989. The obtained correlation was

$$\frac{FF(t)}{FF(0)} = 1.00282 \times \left( \frac{\overline{\mu\tau}_t}{\overline{\mu\tau}_0} \right)^{0.13789} \quad (5.9)$$

The correlation was evaluated with the experimental data and was compared against the Smith model. The results are summarized in Table 5.14 and graphically in Fig. 5.10.

Table 5.14 Evaluation of Correlation Model

	Time hours	Fill Factor ratio	Correlation model	Error %	Smith model	Error %
1000 $W/m^2$ 50° F	0	100.00%	100.28%	0.28%	100.00%	0.00%
	24	91.93%	91.17%	-0.83%	87.73%	-4.57%
	48	88.69%	88.60%	-0.10%	84.05%	-5.23%
	72	86.51%	87.09%	0.67%	81.83%	-5.41%
	96	86.04%	86.03%	-0.02%	80.26%	-6.72%
2000 $W/m^2$ 50° F	0	100.00%	100.28%	0.28%	100.00%	0.00%
	24	88.28%	85.95%	-2.64%	80.14%	-10.15%
	48	85.99%	83.38%	-3.04%	76.25%	-12.77%
1000 $W/m^2$ 120° F	0	100.00%	100.28%	0.28%	100.00%	0.00%
	24	92.19%	90.65%	-1.67%	86.99%	-5.64%
	48	91.10%	88.51%	-2.84%	83.92%	-7.89%
	72	89.75%	87.54%	-2.47%	82.50%	-8.08%
<i>RMSE</i>				1.70%		6.76%

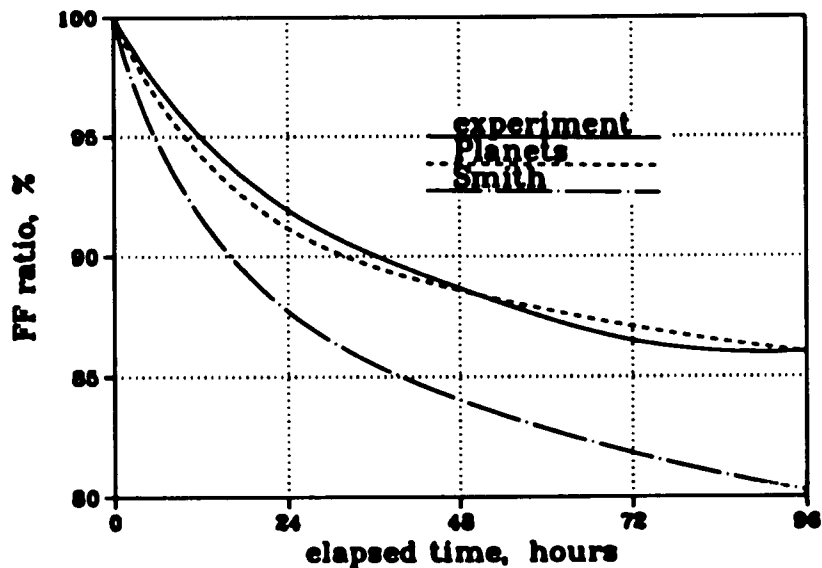


Fig. 5.10 Comparison of Correlation at 1000  $W/m^2$  & 50° F

The observation of the comparison reveals that the correlation model made by the PLANETS is superior to the Smith model. The major reason may be due to the different characteristics of the samples used for the development of the two models.

The experimental data showed that the change in the open-circuit voltage was minor compared to the variation of  $I_{sc}$  and the fill factor. This is consistent with prior work. Therefore, eq. (4.27) is still valid for the samples used. By combining eq. (4.18), (4.27), and (5.9), the relation between the photovoltaic cell efficiency with and without degradation can solely be expressed in terms of the  $\bar{\mu}\tau$  product by the following equation:

$$\frac{\eta}{\eta_o} = 1.00282 \times \left( \frac{\bar{\mu}\tau_t}{\bar{\mu}\tau_o} \right)^{0.13789} \times \frac{\bar{\mu}\tau_t \left[ 1 - \exp\left(\frac{-d^2}{\bar{\mu}\tau_t V_{oc}}\right) \right]}{\bar{\mu}\tau_o \left[ 1 - \exp\left(\frac{-d^2}{\bar{\mu}\tau_o V_{oc}}\right) \right]} \quad (5.10)$$

## 5.6 Discussion

The general features of our results for degradation and recovery processes agree with the results obtained from prior works. The activation energies are also in reasonable agreement with previously published values. As mentioned earlier, the SWE is self-limiting. Therefore, the dangling bond density approaches an equilibrium value after extended time periods. If the light intensity and the temperature are constant, the equilibrium point of the dangling bond density,  $N_{s,\infty}$ , can be found for the steady-state condition (where  $dN_s/dt = 0$  and  $N_{s,\infty} \gg N_s(0)$  in eq. (4.10)) as follows:

$$N_{s,\infty} \approx \left[ \frac{k_d}{k_r} \exp\left[\frac{-(E_{ad} - E_{ar})}{kT}\right] G^2 \right]^{1/4} \quad (5.11)$$

From eq. (5.11), which was developed in this study, it can be seen that the equilibrium value of the dangling bond density is determined by the cell parameters and the ambient conditions. It was also noted that  $N_{s,\infty}$  is independent of the initial dangling bond density before light exposure.

In operating arrays of photovoltaic modules, both the insolation and the module temperature are continually varying. Thus, the  $N_s$  value is continually varying. The objective of the performance model program developed in this study is tracking this continually varying  $N_s$  value. This will be discussed in the next chapter.

## CHAPTER 6

### SIMULATION AND VALIDATION OF THE MODEL

The goal of a simulation study is to develop a model and to validate the model generated results with experimental data. In prior chapters, the mathematical relationships necessary for the prediction of the performance of *a-Si:H* photovoltaic arrays were developed. In this chapter, these equations will be combined in a predictive computer model, which will be validated.

The experimental data from the Solar Energy Research Facility (SERF) at the University of Arizona will be used for the validation. The SERF installation was designed to monitor the performance of amorphous silicon photovoltaic panels (Osborn 1988). The photovoltaic panels at the SERF were made by ARCO Inc. and have characteristics identical to the samples used in the experimental parts of this study.

The entire model consists of four predictive submodels, which are solar radiation, cell temperature, *I-V* curve based performance analysis, as well as an analysis of degradation and recovery. Figure 6.1 shows the schematic of the entire model.

#### **6.1 Simulation of Insolation Incident on Panel**

As discussed previously, direct and diffuse insolation are simulated. Ground reflection is ignored, since the location of the modules relative to each other and

the ground makes this term insignificant. Direct radiation is calculated from eqn (2.12), which is universally accepted. Diffuse radiation is calculated from the Perez model in eqn (2.9), which accounts for the anisotropic nature of diffuse radiation, and is the best radiation model available at this time.

Unfortunately, a complete set of data is not available from the test panel at the SERF for the initial exposure period. Thus, TMY data had to be used instead of actual experimental data for the ambient conditions and insolation. However, since the final data was totalled over monthly time periods, the results were quite reasonable.

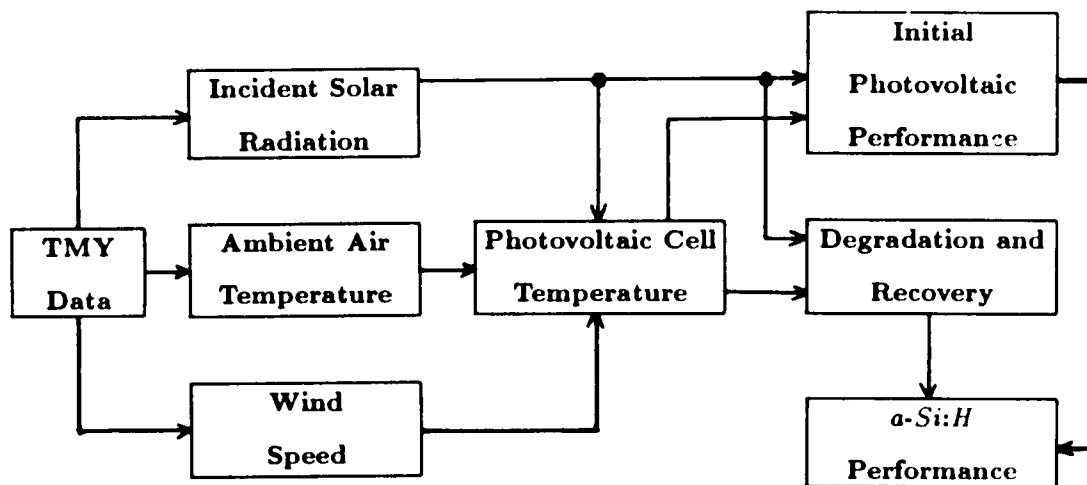


Fig. 6.1 Schematic of the Entire Model

## 6.2 Simulation of Panel Temperature

The temperature of the photovoltaic panel significantly affects the cell performance. Thus, the cell temperature must be calculated for each time period used

in the model, using ambient conditions (insolation, wind speed, ambient temperature) as input data. The cell temperature prediction procedure was discussed in Chapter 3, which is based on the Fuentes model.

However, the dimensionless correlations used in the Fuentes model to determine convective heat transfer coefficients were replaced with a simplified ASHRAE correlation, since the complex array geometry and the resulting local variations in wind speed and direction on the actual structure reduce the significance of specific dimensionless number correlation. The following values were used for the cell performance simulation study (Incropera and DeWitt 1985; Fuentes 1987; ARCO G4000 1988):

- Absorptivity,  $\alpha$ : 0.83
- Cell emissivity,  $\epsilon_c$ : 0.84
- Ground emissivity,  $\epsilon_g$ : 0.90
- Cell density,  $\rho$ :  $446 \text{ kg/m}^3$
- Cell specific heat,  $c$ :  $750 \text{ J/kg} - \text{K}$
- Cell thermal mass,  $mc$ :  $6,150 \text{ J/K}$

The model simulation procedures are:

1. Input G4000 photovoltaic panel specifications, such as thermal mass, density, absorptivity, and emissivity.
2. Compute the actual sky temperature from eq. (3.10).
3. Assume the ground temperature. Since the radiation terms in eq. (3.1) are not significant in comparison with the convective term, the ground temperature,  $T_g$ , was simply assumed to be the same as the dry bulb temperature.
4. Assume the panel temperature,  $T_p$ . As an initial guess,  $T_p$  was assumed to be  $10^\circ \text{F}$  higher than the dry bulb temperature.

5. Solve eq. (3.1) for finding  $T_p$ .
6. Compare the calculated  $T_p$  in step-5 with the assumed  $T_p$  in step-4.
7. If the difference between them is greater than the tolerance ( $2^\circ F$  in this study), go to step-5 with the calculated  $T_p$  as a second guess.
8. Repeat step-7 until the difference is within the tolerance.

To validate the model, the simulation of panel temperature was performed using actual insolation, dry bulb temperature, and wind speed data recorded at the SERF. The actual panel temperatures monitored at the SERF for the period of July 22-25 and August 25-29 were randomly sampled and compared to the simulated results. The root mean square error (*RMSE*) between them was 4.42%. In worst case, the relative error was about 10%, however, mostly within 5%. The comparison is attached in Appendix-B.

The effect of wind on  $T_p$  is important for the prediction of the panel temperature. Figure 6.2 shows the effect. In this study, the empirical ASHRAE correlation was used to predict the convective heat transfer coefficient and the result was very satisfactory.

In contrast, the effect of thermal mass on panel temperature is negligible. For hourly simulation intervals, the panel temperature is solely determined by the average ambient conditions during the time period. Figure 6.3 shows the time required for the panel to come to equilibrium with the ambient conditions, which is far less than the time period of the simulation.

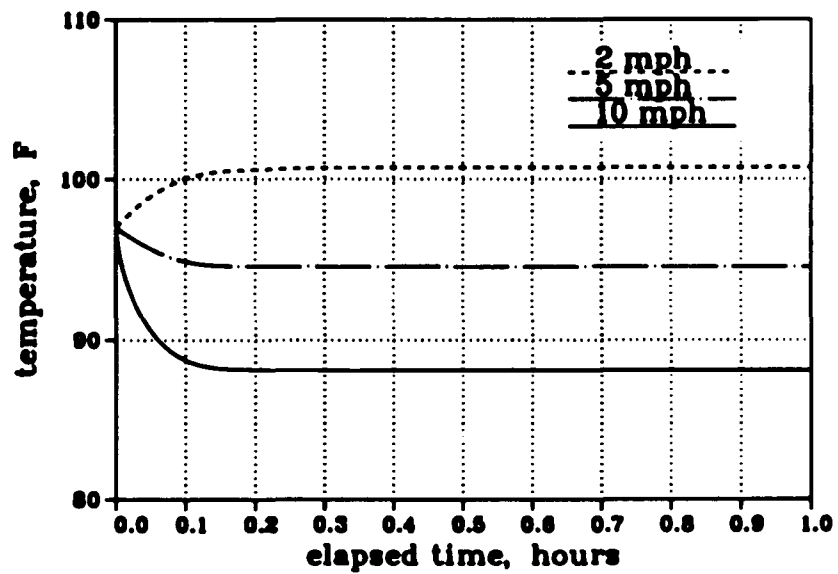


Fig. 6.2 Effect of Wind Speed on Panel Temperature

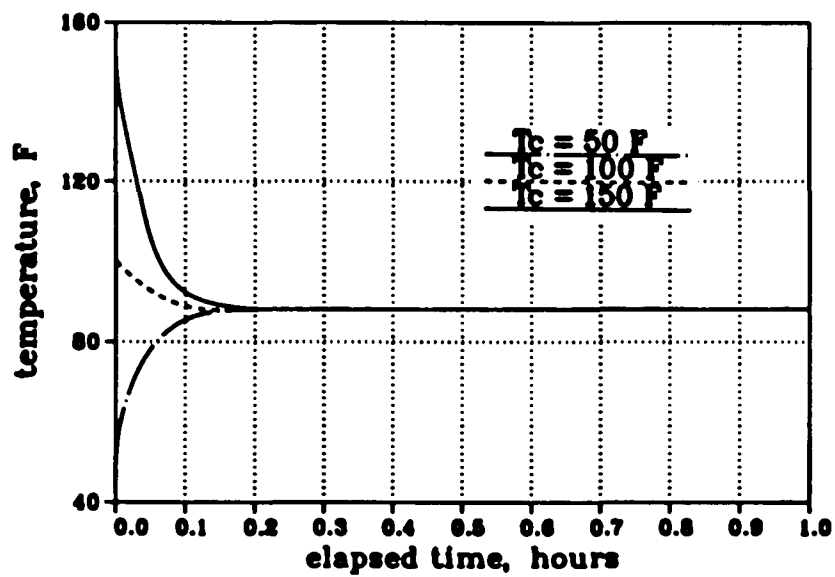


Fig. 6.3 Effect of Initial Panel Temperature

### **6.3 Simulation of the $I$ - $V$ characteristics**

The  $I$ - $V$  characteristics analysis model of the G4000 was written and validated with the manufacturer's  $I$ - $V$  characteristics data, as was discussed in Chapter 3. The model simulation procedure was also explained in Chapter 3. To avoid the SWE for validation of the undegraded panel performance, the initial performance of the SERF photovoltaic array immediately after light exposure was compared with the model generated  $I$ - $V$  characteristics using the SERF solar radiation and panel temperature data on June 13, 1988. The detailed comparison result is attached in Appendix-C. The  $RMSE$  analysis of the difference between the calculated and actual results are:

- Open-circuit voltage,  $V_{oc}$ : 0.60%
- Short-circuit current,  $I_{sc}$ : 3.18%
- Voltage at the maximum power,  $V_m$ : 1.74%
- Current at the maximum power,  $I_m$ : 1.88%
- Fill factor,  $FF$ : 3.85%

Thus, the  $I$ - $V$  characteristics model made in this study satisfactorily predicts the actual performance of the SERF photovoltaic array. After the initial exposure, the photovoltaic performance at the SERF decreased due to the SWE. The degradation data of the SERF and the degradation predicted by the model will be compared in the next section.

### **6.4 Simulation of the SWE**

Validation of this part of the model is not straightforward. The collection of data regarding the SWE in an operating photovoltaic array is a major goal of the

photovoltaic installation at the SERF. Unfortunately, the data for the ambient conditions and array output were recorded sporadically during the first two months of operation. Due to this unavailability of hourly ambient conditions and performance data, TMY data for Tucson was used to run the computer model for comparison with the photovoltaic array output data available from the SERF.

The model simulation procedures are:

1. Input the experimentally determined degradation and recovery parameters in eq. (4.11).
2. Input the panel temperature predicted by the Fuentes model modified with the ASHRAE convective correlation in eq. (4.11).
3. Compute the carrier generation rate,  $G$ , by using hourly solar radiation data generated by the Perez model and eq. (5.1).
4. Compute the dangling bond density from eq. (4.11).
5. Compute the  $\overline{\mu\tau}$  product from eq. (4.3).
6. Compute the degradation in efficiency from eq. (5.10).

Since the values of voltage and current at the maximum power point were available from the SERF, the fill factor and the efficiency can be calculated. The degradation in efficiency,  $D_{eff}$ , then can be expressed as

$$D_{eff} = 1 - \frac{\eta_t}{\eta_o} \quad (6.1)$$

The available SERF data from June 13 (month #6) to November 8 (month #11) in 1988 were analyzed and compared with the model prediction. The comparison for that period is summarized in Table 6.1 and graphically in Fig. 6.4.

Table 6.1 Degradation in Efficiency  
SERF vs Model

Month	SERF	Model	Error
6	0.00%	0.00%	0.00%
7	13.16%	15.99%	21.52%
8	15.96%	17.22%	7.86%
9	17.08%	17.64%	3.30%
10	19.30%	18.43%	-4.50%
11	19.65%	19.50%	0.76%
<i>RMSE</i>			10.55%

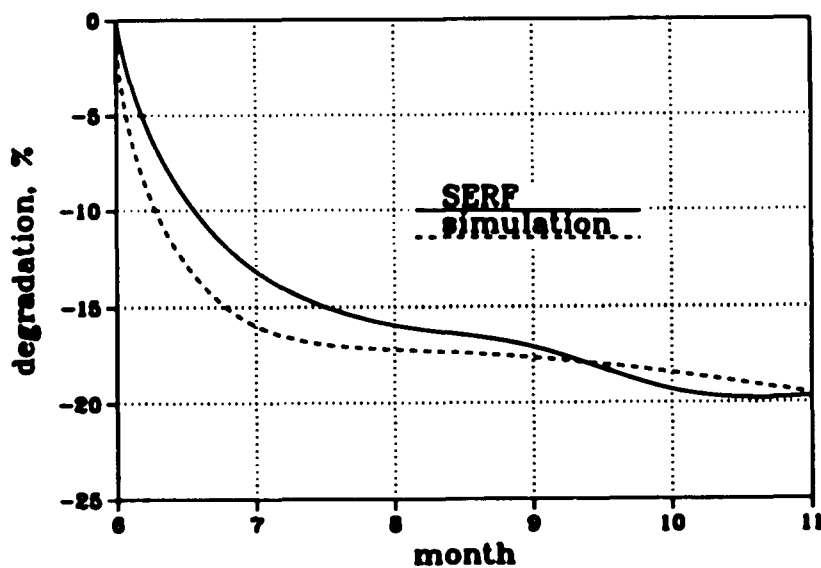


Fig. 6.4 Comparison of Degradation in Efficiency

According to the comparison, the model predicted degradation has turned out to be more rapid than the actual by 20% for the initial month. Since September, however, the model and the actual match very well. The initial discrepancy may involve many things, such as the use of TMY insolation and ambient conditions

data, the experimental error in the determination of the degradation and recovery parameters, and meter reading errors. The comparison on daily basis is attached in Appendix-D. Since the prediction of the long-term array performance is the goal of the program, the excellent match of the model and the SERF data after the first month is encouraging.

The entire model made in this study has been validated against actual SERF performance data for both the initial performance and the subsequent degradation. A close look at the schematic diagram in Fig. 6.1 reveals that the photovoltaic performance with and without the degradation effect can simply be represented in terms of the incident solar radiation and the temperature of the panel. The long-term performance model developed in this study is based on this observation.

### **6.5 Long-Term Performance Model**

As explained in Chapter 4, the two key variables which control the magnitude of the SWE are the intensity of the incident solar radiation and the panel temperature. Therefore, it can be expected that the performance of *a-Si:H* photovoltaic panels can be described as a function of incident radiation and panel temperature. Since the degradation due to incident solar radiation is cumulative in panels exposed to the elements (as they must be), an additional parameter will be required to track the history of panel operation. This parameter is the total radiation incident on the panel over its lifetime.

Thus, the degradation in efficiency can be modeled at the ambient conditions by the following functional relationship:

$$\frac{\eta}{\eta_0} = f(I_{sun}, T_p, \sum I_{sun}) \quad (6.2)$$

where  $\sum I_{sun}$  is the total radiation to which the panel was exposed. The PLANETS program was used to correlate the functional relationship in eq.(6.2). By running PLANETS with the experimental data, the correlation factor was satisfactory, having a value of 0.880. The obtained correlation was

$$\frac{\eta}{\eta_o} = 0.9281 \times I_{sun}^{-0.00746} T_p^{0.03471} \left( \sum I_{sun} \right)^{-0.02072} \quad (6.3)$$

It was noted from eq. (6.3) that the negative power coefficients on solar radiation terms represent degradation, while the positive coefficient on the temperature term reflects the recovery process. This is consistent with the theoretical analysis in Chapter 4. Even though the inclusion of radiation and temperature terms is necessary for an accurate prediction model, the degradation in efficiency was also correlated in terms of the total radiation exposed only by the following equation:

$$\frac{\eta}{\eta_o} = f \left( \sum I_{sun} \right) \quad (6.4)$$

By running PLANETS, the following correlation was obtained with the correlation factor of 0.861:

$$\frac{\eta}{\eta_o} = 1.0644 \times \left( \sum I_{sun} \right)^{-0.02233} \quad (6.5)$$

Equation (5.10) is for the analysis of degradation and recovery processes in terms of carrier lifetime, while eq. (6.5) is designed for the long-term performance prediction model in terms of the solar radiation available. The two correlations were evaluated with the model generated results. The comparison is summarized in Table 6.2.

Table 6.2 Degradation in Efficiency  
Model vs Correlations

Month	Model	Correlation eq. (6.3)	Error	Correlation eq. (6.5)	Error
6	15.99%	15.09%	-5.73%	15.13%	-5.44%
7	17.22%	17.33%	0.68%	17.67%	2.64%
8	17.64%	18.25%	3.48%	18.59%	5.41%
9	18.43%	18.95%	2.75%	19.21%	4.17%
10	19.50%	19.59%	0.42%	19.65%	0.75%
11	20.26%	20.21%	-0.19%	19.98%	-1.36%
12	20.96%	20.65%	-1.42%	20.21%	-3.55%
1	21.60%	20.87%	-3.42%	20.42%	-5.51%
2	21.50%	20.94%	-2.61%	20.60%	-4.23%
3	21.37%	20.88%	-2.26%	20.79%	-2.69%
4	20.87%	20.90%	0.14%	21.00%	0.63%
5	19.66%	20.92%	6.41%	21.19%	7.78%
<i>RMSE</i>			3.16%		4.23%

From Table 6.2, the two correlations fit the model generated results satisfactorily. From the two correlations, it was also found that the recovery effect is very minor compared to degradation because degradation and recovery processes can solely be characterized by the solar radiation exposure. However, recovery does have a small effect, since the correlation including temperature in eq. (6.3) does have a slightly better fit during hot and cold seasons.

Among the four installation/tracking modes used at the SERF, a stationary fixed tilt angle array was used for this simulation study. As mentioned in Chapter 4, the actual electric power generated by  $\alpha$ -Si:H photovoltaic arrays can be calculated by multiplying eq. (6.5) by the power generated from undegraded solar arrays. For 10 year operation of the SERF photovoltaic array, the predicted amount of electricity generation per square meter of panel area calculated by eq. (6.5) is summarized

in Table 6.3, and compared with the initial energy production at the initial undegraded rate, as well as the energy production with degradation predicted by the principle model based on the fundamental rate parameters developed in this study.

Table 6.3 Electricity Generation,  $kWhr/m^2$

Year	Without Degradation	With Degradation	Correlation eq. (6.5)	Error
1	150.39	121.07	121.05	-0.02%
2	150.39	120.75	117.37	-2.80%
3	150.39	120.75	116.00	-3.94%
4	150.39	120.75	115.11	-4.67%
5	150.39	120.73	114.47	-5.18%
6	150.39	120.75	113.97	-5.62%
7	150.39	120.75	113.54	-5.97%
8	150.39	120.75	113.16	-6.29%
9	150.39	120.73	112.85	-6.53%
10	150.39	120.75	112.59	-6.67%
<b>Total</b>	<b>1504</b>	<b>1208</b>	<b>1150</b>	
<b>RMSE</b>				<b>4.78%</b>

From Table 6.3, it can be seen that electricity generation with degradation causes 20% losses compared to that without degradation. Since photovoltaic arrays are mostly degraded in the initial month upon light exposure, electricity generation is reasonably stable over a ten year period of operation. According to the correlation in eq. (6.5), electricity generation is slightly decreasing, which results deviating about 5% from the original model.

It is possible that the model based on eq. (6.5) will prove to be more accurate in the long-term. Alternating degradation and recovery processes result in a gradually increasing non-recoverable degradation of performance, which is not

accounted for in the complex principle model developed in this study. In prior discussion, the experimental fact that the recovery process never returns a sample to its initial state is noted, which is the basis of the above postulate.

## CHAPTER 7

### SUMMARY AND CONCLUSIONS

The goal of this study was to develop an analytical model for the prediction of the long-term performance and degradation of amorphous silicon photovoltaic arrays using TMY data for Tucson. By utilizing, synthesizing, and integrating information from widely disparate sources, a predictive model which generates realistic prediction results was written.

This work showed that a model using physically realistic fundamental rate controlling parameters can accurately model the long-term performance of photovoltaic cells where two competing processes vary with temperature and time. Furthermore, it showed the possibility of modeling by separating the calculations into those without degradation, and then modifying them with terms that account for degradation and recovery. This novel approach greatly simplified the mathematical relationships, since the resultant ratios cancelled out many of the difficult variables.

This approach also led to the development of a simple method of the experimental determination of the fundamental rate controlling parameters of degradation and recovery. The ratio based relationships developed in this work permit the evaluation of changes in the carrier lifetime and dangling bond density from simple measurements of  $I_{sc}$ , which in turn allow the calculation of the above parameters. The values of these parameters which were calculated in this work are in reasonable agreement with previously published values by other researchers.

Annealing *a-Si:H* silicon samples showed that the percent recovery from the degraded state to the as-grown state by annealing is virtually independent of the initial state at the start of the annealing process. This permits the independent determination of the recovery rate parameters. When the recovery rate parameters are determined, the degradation rate parameters can be determined from experimental data taken at room temperature. This work showed that the experimental determination of degradation activation energies at very low temperatures is not necessary.

A major result of this work was the development of an extremely simple and fast running algorithm for the long-term performance in terms of the incident solar radiation, the panel temperature, and the total radiation exposed. This correlation was developed by manipulating the results obtained by the analytical and experimental study with the PLANETS software. More importantly, this work showed that the entire process of the SWE could adequately be represented by a correlation in which degradation is solely a function of the total radiation to which the panel is exposed. That implies that the recovery effect is very minor compared to the light-induced degradation. The above two correlations are very satisfactory and have short running times.

From the long-term performance model, it is possible to extend the above results to obtain economic performance indicators for the optimization of *a-Si:H* photovoltaic systems under various operating conditions and design parameters.

**APPENDIX A**

**ASHRAE METHOD**

At the earth's surface on a clear day, the instantaneous direct normal solar radiation per unit area,  $I_{DN}$ , is represented by

$$I_{DN} = A \exp\left(\frac{-B}{\sin \alpha}\right) = A \exp\left[(-B) \times (\text{air mass})\right] \quad (1)$$

where  $A$  is the apparent solar radiation at air mass = 0 in  $Btu/hr-ft^2$ ;  $B$  is the dimensionless atmospheric extinction coefficient.

The direct radiation component on a tilted surface,  $I_{bt}$ , can be expressed by

$$I_{bt} = I_{DN} \cos \theta \quad (2)$$

The diffuse solar radiation that falls on any surface is approximated by

$$I_{dt} = C I_{DN} \left(\frac{1 + \cos \beta}{2}\right) \quad (3)$$

where  $C$  is the ratio of diffuse to direct normal radiation on a horizontal surface.

On a clear day, the attenuation of solar radiation is clearly dependent on the length of the path of the rays through the atmosphere where the absorption and the scattering occur. The air mass term in eqn (1) reflects this effect. The values of  $A$  and  $B$  are generated for the twenty-first day of each month and are representative values for average cloudiness days for latitudes 0 to 64° North. The parameter  $C$  does not account for the actual directional variation of the diffuse component nor its value on cloudy days. The ASHRAE coefficients are given in Table 1.

Table 1 ASHRAE Coefficients

Month	<i>A</i>	<i>B</i>	<i>C</i>
Jan	390	.142	.058
Feb	385	.144	.060
Mar	376	.156	.071
Apr	360	.180	.097
May	350	.196	.121
Jun	345	.205	.134
Jul	344	.207	.136
Aug	351	.201	.122
Sep	365	.177	.092
Oct	378	.160	.073
Nov	387	.149	.063
Dec	391	.142	.057

**APPENDIX B**

**COMPARISON OF EXPERIMENTAL AND  
CALCULATED PANEL TEMPERATURE**

**Array-A Temperature Comparison**

Date	Time	SERF temperature °F	Calculated temperature °F	Relative error	Squared relative error
7-22	16:00	131	132	0.84%	0.01%
7-22	17:00	126	126	0.40%	0.00%
7-22	18:00	116	114	-1.47%	0.02%
7-22	19:00	96	99	2.91%	0.08%
7-23	7:00	79	78	-1.02%	0.01%
7-23	8:00	96	94	-2.49%	0.06%
7-23	11:00	137	134	-2.33%	0.05%
7-23	12:00	137	134	-1.83%	0.03%
7-23	13:00	136	136	-0.07%	0.00%
7-23	16:00	101	106	5.16%	0.27%
7-23	17:00	95	102	7.03%	0.49%
7-23	18:00	98	105	6.82%	0.46%
7-23	19:00	101	106	5.16%	0.27%
7-24	7:00	81	82	1.74%	0.03%
7-24	8:00	98	102	4.29%	0.18%
7-24	9:00	117	118	0.51%	0.00%
7-24	11:00	130	137	5.79%	0.34%
7-24	12:00	133	132	-0.60%	0.00%
7-24	13:00	137	133	-2.71%	0.07%
7-24	14:00	134	133	-0.82%	0.01%
7-24	15:00	134	127	-5.01%	0.25%
7-24	16:00	128	125	-2.04%	0.04%
7-24	17:00	125	125	0.24%	0.00%
7-24	18:00	108	109	1.40%	0.02%
7-24	19:00	74	81	9.31%	0.87%
7-25	7:00	78	76	-1.94%	0.04%
7-25	8:00	88	89	1.14%	0.01%
7-25	9:00	115	111	-3.39%	0.12%
7-25	10:00	135	128	-5.40%	0.29%
7-25	11:00	134	132	-1.79%	0.03%
7-25	12:00	135	134	-0.74%	0.01%
7-25	13:00	133	136	2.18%	0.05%
7-25	14:00	140	136	-2.72%	0.07%
7-25	15:00	139	136	-1.88%	0.04%
7-25	16:00	134	132	-1.20%	0.01%
7-25	17:00	124	125	0.64%	0.00%
7-25	18:00	114	116	2.02%	0.04%
7-25	19:00	100	105	5.11%	0.26%

**Array-A Temperature Comparison**

Date	Time	SERF temperature °F	Calculated temperature °F	Relative error	Squared relative error
8-25	8:00	85	88	3.41%	0.12%
8-25	9:00	108	104	-3.61%	0.13%
8-25	10:00	128	118	-7.67%	0.59%
8-25	11:00	142	128	-9.54%	0.91%
8-25	12:00	139	130	-6.47%	0.42%
8-25	13:00	142	134	-5.90%	0.35%
8-25	14:00	139	131	-5.42%	0.29%
8-25	15:00	141	135	-3.98%	0.16%
8-25	16:00	131	124	-5.34%	0.29%
8-25	17:00	125	118	-5.45%	0.30%
8-25	18:00	107	106	-1.12%	0.01%
8-25	19:00	90	92	1.77%	0.03%
8-26	8:00	89	87	-1.92%	0.04%
8-26	9:00	112	106	-5.02%	0.25%
8-26	10:00	132	121	-8.19%	0.67%
8-26	11:00	138	128	-7.51%	0.56%
8-26	12:00	142	132	-6.85%	0.47%
8-26	13:00	139	135	-2.67%	0.07%
8-26	14:00	130	119	-8.25%	0.68%
8-26	15:00	104	99	-4.53%	0.21%
8-26	16:00	96	94	-2.19%	0.05%
8-26	17:00	95	94	-1.16%	0.01%
8-26	18:00	91	91	-0.44%	0.00%
8-27	7:00	77	77	-0.52%	0.00%
8-27	8:00	88	86	-2.27%	0.05%
8-27	9:00	102	98	-3.73%	0.14%
8-27	10:00	86	84	-2.44%	0.06%
8-27	11:00	81	78	-4.18%	0.17%
8-27	12:00	91	88	-2.76%	0.08%
8-27	13:00	118	106	-9.79%	0.96%
8-27	14:00	136	128	-5.88%	0.35%
8-27	15:00	137	128	-6.36%	0.41%
8-27	16:00	120	119	-1.16%	0.01%
8-27	17:00	88	89	1.48%	0.02%
8-28	7:00	73	73	-0.14%	0.00%
8-28	8:00	87	86	-1.49%	0.02%
8-28	9:00	104	99	-4.99%	0.25%
8-28	10:00	116	108	-7.14%	0.51%

**Array-A Temperature Comparison**

Date	Time	SERF temperature °F	Calculated temperature °F	Relative error	Squared relative error
8-28	12:00	130	120	-7.98%	0.64%
8-28	13:00	141	132	-6.18%	0.38%
8-28	14:00	144	133	-7.83%	0.61%
8-28	15:00	140	129	-7.66%	0.59%
8-28	16:00	133	128	-4.05%	0.16%
8-28	17:00	109	108	-0.46%	0.00%
8-28	18:00	94	98	3.92%	0.15%
8-28	19:00	87	90	3.45%	0.12%
8-29	8:00	85	85	-0.23%	0.00%
8-29	9:00	94	94	-0.42%	0.00%
8-29	10:00	106	103	-3.01%	0.09%
8-29	13:00	127	121	-4.42%	0.20%
8-29	15:00	131	125	-4.29%	0.18%
<i>RMSE</i>					4.42%

**APPENDIX C****COMPARISON OF EXPERIMENTAL AND  
CALCULATED  $I$ - $V$  CHARACTERISTICS**

### Array-A *I-V* Characteristics Comparison

(SERF Data)

#	Date	Time	$V_{oc}$ volts	$I_{sc}$ amps	$V_m$ volts	$I_m$ amps	$FF$
A1	6-13	12.5	61.5	2.24	45.0	1.87	0.611
A2	6-13	14.2	61.4	2.19	45.0	1.81	0.606
A3	6-13	12.0	60.4	2.27	45.0	1.90	0.624
A4	6-13	11.9	61.1	2.25	45.0	1.92	0.628
A5	6-13	12.7	61.3	2.24	45.0	1.90	0.623
A6	6-13	12.8	61.6	2.24	45.0	1.87	0.610
A7	6-13	13.0	61.0	2.24	45.0	1.87	0.616
A8	6-13	13.2	60.7	2.24	45.0	1.87	0.619

(Calculated)

#	Date	Time	$V_{oc}$ volts	$I_{sc}$ amps	$V_m$ volts	$I_m$ amps	$FF$
A1	6-13	12.5	61.7	2.31	46.0	1.85	0.596
A2	6-13	14.2	61.8	2.27	46.2	1.81	0.598
A3	6-13	12.0	60.8	2.32	45.2	1.86	0.594
A4	6-13	11.9	61.6	2.31	45.9	1.85	0.596
A5	6-13	12.7	61.6	2.31	45.9	1.85	0.596
A6	6-13	12.8	61.6	2.32	45.8	1.86	0.595
A7	6-13	13.0	60.8	2.32	45.2	1.86	0.594
A8	6-13	13.2	61.3	2.33	45.6	1.86	0.595

(Error Analysis)

#	Date	Time	$V_{oc}$ volts	$I_{sc}$ amps	$V_m$ volts	$I_m$ amps	$FF$
A1	6-13	12.5	0.32%	3.03%	2.17%	-1.08%	-2.49%
A2	6-13	14.2	0.65%	3.52%	2.60%	0.00%	-1.29%
A3	6-13	12.0	0.66%	2.16%	0.44%	-2.15%	-4.98%
A4	6-13	11.9	0.81%	2.60%	1.96%	-3.78%	-5.45%
A5	6-13	12.7	0.49%	3.03%	1.96%	-2.70%	-4.47%
A6	6-13	12.8	0.00%	3.45%	1.75%	-0.54%	-2.50%
A7	6-13	13.0	-0.33%	3.45%	0.44%	-0.54%	-3.68%
A8	6-13	13.2	0.98%	3.86%	1.32%	-0.54%	-4.02%
<i>RMSE</i>			0.60%	3.16%	1.74%	1.88%	3.85%

**APPENDIX D****COMPARISON OF EXPERIMENTAL DEGRADATION DATA**  
**WITH CALCULATED DEGRADATION VALUES**

## SERF June-July-August Data

panel area: 113,527 cm<sup>2</sup>

Date	Time	Rad W/m <sup>2</sup>	V <sub>m</sub> volts	I <sub>m</sub> amps	SERF η	SERF η degraded	Calc η ratio	Calc η degraded
initial					5.70%			
6-13	14	1031	45.0	13.76	5.29%	7.19%	0.911	8.90%
6-16	10	958	45.0	13.29	5.50%	3.53%	0.879	12.10%
6-21	12	991	45.0	13.15	5.26%	7.72%	0.963	13.70%
6-25	11	1040	42.0	14.37	5.11%	10.32%	0.856	14.40%
6-26	11	967	42.0	13.43	5.14%	9.86%	0.855	14.50%
6-27	12	980	42.0	13.60	5.13%	9.93%	0.853	14.70%
6-30	11	974	45.0	12.65	5.15%	9.68%	0.850	15.00%
7- 2	12	986	42.0	13.59	5.10%	10.54%	0.848	15.20%
7- 6	9	954	42.0	13.14	5.10%	10.60%	0.845	15.50%
7- 9	13	969	42.0	13.47	5.14%	9.78%	0.843	15.70%
7-14	13	975	42.0	13.05	4.95%	13.16%	0.840	15.99%
7-22	16	742	33.0	12.52	4.90%	13.95%	0.836	16.40%
7-23	12	928	33.0	15.56	4.87%	14.51%	0.835	16.50%
7-24	12	935	34.5	15.38	5.00%	12.33%	0.835	16.50%
7-25	12	933	34.5	14.87	4.85%	14.99%	0.835	16.50%
8-17	14	925	34.9	14.40	4.79%	15.96%	0.828	17.22%
8-18	12	605	33.9	9.72	4.79%	15.96%	0.828	17.22%
8-19	12	1047	35.7	16.16	4.86%	14.74%	0.826	17.40%
8-20	11	311	33.2	5.23	4.91%	13.86%	0.826	17.40%
8-22	15	755	33.4	11.96	4.66%	18.25%	0.825	17.50%
8-23	11	887	33.5	14.21	4.73%	17.02%	0.825	17.50%
8-24	13	960	35.2	14.17	4.57%	19.82%	0.825	17.50%
8-25	12	943	35.5	13.63	4.52%	20.70%	0.825	17.50%
8-26	12	934	35.7	13.03	4.39%	22.98%	0.824	17.60%
8-27	12	319	34.5	4.88	4.64%	18.60%	0.824	17.60%
8-28	12	909	35.6	12.46	4.30%	24.56%	0.824	17.60%
8-29	13	963	36.3	13.39	4.45%	21.93%	0.824	17.60%
8-30	12	892	36.6	12.55	4.53%	20.53%	0.823	17.70%
8-31	14	878	36.7	12.60	4.64%	18.60%	0.823	17.70%

## SERF September Data

panel area: 113,527 cm<sup>2</sup>

Date	Time	Rad W/m <sup>2</sup>	V <sub>m</sub> volts	I <sub>m</sub> amps	SERF η	SERF η degraded	Calc η ratio	Calc η degraded
9- 1	10	778	35.7	11.23	4.54%	20.40%	0.822	17.80%
9- 2	12	971	35.1	14.58	4.64%	18.51%	0.822	17.80%
9- 3	10	332	40.1	4.31	4.58%	19.65%	0.822	17.80%
9- 5	12	798	41.1	10.38	4.71%	17.37%	0.823	17.70%
9- 6	12	977	43.4	11.71	4.58%	19.65%	0.823	17.70%
9- 7	12	970	42.9	11.96	4.66%	18.25%	0.823	17.70%
9- 8	13	962	41.2	12.56	4.74%	16.84%	0.823	17.70%
9- 9	11	860	38.7	11.86	4.70%	17.54%	0.823	17.70%
9-10	12	954	39.4	12.40	4.51%	20.88%	0.823	17.70%
9-11	12	372	38.8	5.17	4.75%	16.67%	0.823	17.70%
9-12	13	974	39.4	13.16	4.69%	17.72%	0.823	17.70%
9-13	12	968	40.1	13.09	4.78%	16.14%	0.823	17.70%
9-14	11	948	39.6	12.80	4.71%	17.37%	0.824	17.64%
9-15	12	1000	39.6	13.44	4.69%	17.72%	0.823	17.70%
9-16	12	991	39.2	13.54	4.72%	17.19%	0.823	17.70%
9-17	12	982	39.8	12.77	4.56%	20.00%	0.822	17.80%
9-18	12	1000	41.0	12.52	4.52%	20.70%	0.822	17.80%
9-19	12	971	41.6	12.27	4.63%	18.77%	0.821	17.90%
9-20	12	347	40.6	4.69	4.84%	15.09%	0.821	17.90%
9-21	12	856	41.0	11.11	4.69%	17.72%	0.820	18.00%
9-22	12	945	41.8	11.91	4.64%	18.60%	0.820	18.00%
9-23	12	990	42.1	12.92	4.84%	15.09%	0.819	18.10%
9-24	12	965	44.3	11.67	4.72%	17.19%	0.819	18.10%
9-25	12	952	44.2	11.74	4.81%	15.61%	0.818	18.20%
9-26	12	952	40.5	12.66	4.74%	16.84%	0.818	18.20%
9-27	12	952	43.2	11.53	4.61%	19.12%	0.818	18.20%
9-28	12	963	43.4	12.61	5.00%	12.28%	0.817	18.30%
9-29	12	922	33.9	14.25	4.62%	18.95%	0.817	18.30%
9-30	12	959	32.6	15.55	4.65%	18.42%	0.816	18.40%

## SERF October-November Data

panel area: 113,527 cm<sup>2</sup>

Date	Time	Rad W/m <sup>2</sup>	V <sub>m</sub> volts	I <sub>m</sub> amps	SERF η	SERF η degraded	Calc η ratio	Calc η degraded
10- 1	12	975	40.2	12.81	4.65%	18.42%	0.816	18.40%
10- 2	12	968	39.9	12.81	4.65%	18.42%	0.816	18.40%
10- 3	12	945	39.3	12.86	4.71%	17.37%	0.816	18.40%
10- 4	12	818	39.3	11.48	4.86%	14.74%	0.816	18.40%
10- 5	12	930	39.2	12.74	4.73%	17.02%	0.816	18.40%
10- 6	12	941	36.4	13.47	4.59%	19.47%	0.816	18.40%
10- 7	12	950	37.2	12.87	4.44%	22.11%	0.816	18.40%
10- 8	12	590	37.0	8.35	4.61%	19.12%	0.816	18.40%
10- 9	12	921	37.0	13.71	4.85%	14.91%	0.816	18.40%
10-11	15	725	36.6	9.82	4.37%	23.33%	0.816	18.40%
10-12	12	918	37.1	13.00	4.63%	18.77%	0.816	18.40%
10-13	12	871	36.9	12.25	4.57%	19.82%	0.816	18.43%
10-27	12	899	40.8	11.50	4.60%	19.30%	0.808	19.20%
10-28	12	888	40.5	11.34	4.56%	20.00%	0.808	19.20%
10-29	12	895	40.3	11.39	4.52%	20.70%	0.807	19.30%
10-30	12	295	38.4	4.00	4.58%	19.65%	0.807	19.30%
10-31	12	911	39.7	12.03	4.62%	18.95%	0.806	19.40%
11- 1	12	918	39.6	12.06	4.58%	19.58%	0.806	19.40%
11- 2	12	901	39.5	11.87	4.58%	19.60%	0.806	19.40%
11- 3	12	899	40.0	11.72	4.59%	19.45%	0.806	19.40%
11- 4	12	893	40.9	11.53	4.65%	18.42%	0.806	19.40%
11- 5	12	893	39.9	11.76	4.63%	18.77%	0.805	19.50%
11- 6	12	894	41.4	11.53	4.70%	17.54%	0.805	19.50%
11- 7	12	762	64.4	6.18	4.60%	19.30%	0.805	19.50%
11- 8	12	896	41.6	11.19	4.58%	19.65%	0.805	19.50%

## REFERENCES

- Angrist,S.W., *Direct Energy Conversion*, 4th ed., Allyn and Bacon, Inc., 1982, pp.175-176.
- ARCO Solar Installation Guide, For the G4000 Solar Electric Module, ARCO Solar Inc., 1988.
- Araujo,G.L. and Sanchez,E., "Analytical Expressions for the Determination of the Maximum Power Point and the Fill Factor of a Solar Cell", *Solar Cells*, 5, 1982, pp.377-386.
- ASHRAE Handbook of Fundamentals, American Society of Heating, Refrigerating, and Air Conditioning Engineers, Atlanta, GA, 1981, pp.2.14-2.15, 27.2-27.9.
- Bahm,R.J., TMY Data Handbook, Microcomputer Design Tools Inc., Albuquerque, NM, 1985.
- Baltas,P., Tortoreli,M., and Russell,P.E., "Evaluation of Power Output for Fixed and Step Tracking Photovoltaic Arrays", *Solar Energy*, 37, 2, 1986, pp.147-163.
- Bennett,M.S., Arya,R.R., Newton,J.L., Catalano,A., and Rajan,K., "Kinetics of Light-induced Degradation and Thermal Annealing of *a-Si:H* Solar Cells", *Conf. Rec. of the 18th IEEE Photovoltaic Specialists Conf.*, 1985, pp.1584-1587.
- Bhargava,B., Bhatnagar,A.K., and Karihaloo,R.K., "Degradation in Power Output of Amorphous Silicon Modules on Field Exposure", *Conf. Rec. of the 19th IEEE Photovoltaic Specialists Conf.*, 1987, pp.1441-1444.
- Buresh,M., *Photovoltaic Energy Systems: Design and Installation*, McGraw-Hill, 1983, pp.72-73.
- Carlson,D.E., Wronski,C.R., Triano,A.R., and Daniel,R.E., "Solar Cells using Schottky Barriers on Amorphous Silicon", *Conf. Rec. of the 12th IEEE Photovoltaic Specialists Conf.*, 1976, pp.893-895.
- Crandall,R.S., "Transport in Hydrogenated Amorphous Silicon *p-i-n* Solar Cells", *J. Applied Physics*, 53(4), 1982, pp.3350-3352.

- Crandall,R.S., "Modeling of Thin Film Solar Cells: Uniform Field Approximation", *J. Applied Physics*, 54(12), 1983, pp.7176-7186.
- Czubatyj,W., Shur,M., Ng,K., and Madan,A., "Photovoltaic Behavior of Amorphous Silicon-Based Alloys", *Conf. Rec. of the 14th IEEE Photovoltaic Specialists Conf.*, 1980, pp.1214-1217.
- Dave,J.V., "Validity of the Isotropic-Distribution Approximation in Solar Energy Estimations", *Solar Energy*, 19, 1977, pp.331-333.
- DeBlasio,R., Waddington,D., and Mrig,L., "Outdoor Performance and Stability Testing of Thin Film Devices", *Solar Cells*, 21, 1987, pp.343-351.
- Dressnandt,N.C. and Rothwarf,A., "Limits to the Open Circuit Voltage of *a-Si:H* *p-i-n* Solar Cells", *Conf. Rec. of the 17th IEEE Photovoltaic Specialists Conf.*, 1984, pp.364-368.
- Duffie,J.A. and Beckman,W.A, *Solar Engineering of Thermal Processes*, John Wiley & Sons, Inc., 1980, pp.3-22.
- Eser,E., "Light Induced Degradation and Thermal Recovery of the Photoconductivity in Hydrogenated Amorphous Silicon Films", *J. Applied Physics*, 59(10), 1986, pp.3508-3515.
- Eser,E., Ramaprasad,K.R., Volltrauer,H., Ramos,F., Gau,S.C., and Vos,R., "Long Term Stability of Amorphous Silicon Solar Cells and Modules", *Solar Cells*, 21, 1987, pp.25-39.
- Faughnan,B.W. and Crandall,R.S., "Determination of Carrier Collection Length and Prediction of Fill Factor in Amorphous Silicon Solar Cells", *Appl. Phys. Lett.*, 44(5), 1984, pp.537-539.
- Ferziger,J.H., *Numerical Methods for Engineering Application*, John Wiley & Sons, Inc., 1981, pp.57-62.
- Fuentes,M.K., "A Simplified Thermal Model for Flat-plate Photovoltaic Arrays", Sandia Report SAND85-0330.UC-63, 1987.
- Green,M.A., *Solar Cells*, Prentice Hall, Inc., Englewood Cliffs, NJ, 1982, pp.88-89, 153.
- Hack,M. and Shur,M., "Implication of Light-induced Defects on the Performance of

- Amorphous Silicon Alloy *p-i-n* Solar Cells", *Conf. Rec. of the 18th IEEE Photovoltaic Specialists Conf.*, 1985, pp.1588-1593.
- Hamakawa, Y., Current Topics in Photovoltaics, Edited by Coutts, T.J. and Meakin, J.D., Academic Press, 1985, pp.130-144.
- Harrison, A.W. and Coombes, C.A., "Performance Validation of the Perez Tilted Surface Irradiance Model", *Solar Energy*, 42, 4, 1989, pp.327-333.
- Hart, P.R., "Crystalline vs. Amorphous Silicon - A Comparison of Their Respective Properties and Their Significance in Photovoltaic Applications", *7th E.C. Photovoltaic Solar Energy Conf., Proceedings of the International Conf.*, 1986, pp.27-31.
- Hay, J.E., "Study of Shortwave Radiation on Non-Horizontal Surfaces", Rep. 79-12, Atmospheric Environment Service, Downsview, Ontario, 1979.
- Hecht, K., "Zum Mechanismus des Lichtelektrischen Primärstromes in Isolierenden Kristallen", *Zeitschrift für Physik*, 77, 1932, pp.235-245.
- Hester, H. and Hoff, T., "Long-Term Module Performance", *Conf. Rec. of the 18th IEEE Photovoltaic Specialists Conf.*, 1985, pp.198-202.
- Ichikawa, Y., Nabeta, O., Maruyama, K., Ihara, T., Yoshida, T., Sakai, H., Uchida, Y., "Long Term Experimental Tests and Analysis of Single Junction *a-Si* Photovoltaic System", AIP Conference Proceedings 157 - Stability of Amorphous Silicon Alloy Materials and Devices, Stafford, B.L. and Sabisky, E., ed., 1987, pp.318-325.
- Incropera, F.P. and DeWitt, D.A., Introduction to Heat Transfer, John Wiley & Sons, 1985, pp.692-693.
- Klucher, T.M., "Evaluation of Models to Predict Insolation on Tilted Surfaces", *Solar Energy*, 23, 1979, pp.111-114.
- Knobloch, J., Kunzelmann, S., Voss, B., Wilson, H.R., and Wittwer, V., "Efficiency Measurements of Different Types of Solar Cells in Dependence on the Irradiation Conditions", *5th E.C. Photovoltaic Solar Energy Conf., Proceedings of the International Conf.*, 1983, pp.652-656.
- Kuwano, Y., Ohnishi, M., Nishiwaki, H., Tsuda, S., Shibuya, H., and Nakano, S., "Photovoltaic Behavior of Amorphous *Si:H* and *Si:F:H* Solar Cells", *Conf. Rec. of*

- the 15th IEEE Photovoltaic Specialists Conf.*, 1981, pp.698-703.
- Lee,C., Ohlsen,W.D., Taylor,P.C., Ullal,H.S. and Ceasar,G.P., "Kinetics of the Metastable Optically Induced ESR in *a-Si:H*", *Physical Review B.*, 31(1), 1985, pp.100-105.
- Liu,B.Y.H. and Jordan,R.C., "The Interrelationships and Characteristic Distribution of Direct, Diffuse, and Total Radiation", *Solar Energy*, 4(3), 1960, pp.1-19.
- Liu,B.Y.H. and Jordan,R.C., "The Long-Term Average Performance of Flat-Plate Solar-Energy Collectors", *Solar Energy*, 7(2), 1963, pp.53-74.
- Ma,C.C.Y. and Iqbal,M., "Statistical Comparison of Solar Radiation Correlations", *Solar Energy*, 33, 2, 1984, pp.143-148.
- Ma,C.C.Y. and Iqbal,M., "Statistical Comparison of Models for Estimating Solar Radiation on Inclined Surfaces", *Solar Energy*, 31, 1983, pp.313-317.
- Maruska,H.P., Moustakas,T.D., and Hicks,M.C., "Effect of Optical Stress on the Properties of Sputtered Amorphous Silicon Solar Cells and Thin Films", *Solar Cells*, 9, 1983, pp.37-51.
- Mitchell,K.W., Tanner,D., Vasquez,S., Willett,D., and Lewis,S., "Device Characterization and Analysis of Thin Film Silicon:Hydrogen Solar Cells", *Conf. Rec. of the 18th IEEE Photovoltaic Specialists Conf.*, 1985, pp.914-919.
- Moller,M., Rauscher,B., Kruhler,W., Plattner,R., and Pfeiderer,H., "Low-level Boron Doping and Light-induced Effects in Amorphous Silicon *p-i-n* Solar Cells", *Conf. Rec. of the 16th IEEE Photovoltaic Specialists Conf.*, 1982, pp.1376-1380.
- Mrig,L., Rummel,S., and Waddington,D., "Long Term Performance Testing of Amorphous Silicon Modules under Natural Sunlight", AIP Conference Proceedings 157 - Stability of Amorphous Silicon Alloy Materials and Devices, Stafford,B.L. and Sabisky,E. ed., 1987, pp.326-333.
- Mrig,L., Rummel,S., Waddington,D., and DeBlasio,R., "Outdoor Stability Performance of Amorphous Silicon Modules", *Solar Cells*, 24, 1988, pp.381-386.
- Nakano,S., Fukatsu,T., Nishiwaki,H., Shibuya,H., Tsukamoto,K., and Kuwano,Y., "A 2kW Photovoltaic Power Generating System Using *a-Si* Solar Cells", *Conf. Rec. of the 16th IEEE Photovoltaic Specialists Conf.*, 1982, pp.1124-1128.

- Osborn,D.E., Photovoltaic Research Laboratory at the Solar Energy Research Facility University of Arizona, Project Report, August 1988.
- Otterbein,R.T., Evans,D.L., and Facinelli,W.A., "A Modified Single Diode Model for High Illumination Solar Cells for Simulation Work", *Conf. Rec. of the 13th IEEE Photovoltaic Specialists Conf.*, 1978, pp.1074-1079.
- Perez,R., Seals,R., and Stewart,R., "Modeling Irradiance on Tilted Planes: A Simplified Version of the Perez Model; US-wide Climatic/Environmental Evaluation", *Proceedings of the Biennial Meeting of International Solar Energy Society*, Hamburg, FRG, 1987.
- Perez,R., Stewart,R., Arbogast,C., Seals,R., and Scott,J., "An Anisotropic Hourly Diffuse Radiation Model for Sloping Surfaces: Description, Performance Validation, Site Dependency Evaluation", *Solar Energy*, 36, 1986, pp.481-497.
- PLANETS, Programming Language for the Analysis of Economic Time Series, Version 13G, The Brookings Institution, 1984.
- Rauschenbach,H.S., Solar Cell Array Design Handbook, Van Nostrand Reinhold Company, 1980, pp.55,390-391.
- Sakai,H. and Uchida,Y, "Current Progress Towards Reducing Light-Induced Degradation in *a-Si:H* Films and Solar Cells", *Solar Cells*, 22, 1987, pp.275-285.
- Shepard,K., Smith,Z., Aljishi,S., and Wagner,S., "Kinetics of the Generation and Annealing of Deep Defects and Recombination Centers in Amorphous Silicon", *Appl. Phys. Lett.*, 53(17), 1988, pp.1644-1646.
- Shufflebotham,P.K. and Card,H.C., "A Review of Amorphous Silicon Alloys", *J. Non-Cryst. Solids*, 92, 1987, pp.183-244.
- Smietana,P.J., Flocchini,R.G., Kennedy,R.L., and Hatfield,J.L., "A New Look at the Correlation of  $K_d$  and  $K_t$  Ratios and at Global Solar Radiation Tilt Models Using One-Minute Measurements", *Solar Energy*, 32, 1, 1984, pp.99-107.
- Smith,Z.E. and Wagner,S., "Intrinsic Dangling-bond Density in Hydrogenated Amorphous Silicon", *Physical Review B.*, 32(8), 1985, pp.5510-5513.
- Smith,Z.E., Wagner,S., and Faughnan,B.W., "Carrier Lifetime Model for the Optical Degradation of Amorphous Silicon Solar Cells", *Appl. Phys. Lett.*, 46(11), 1985, pp.1078-1080.

- Spear, W.E. and LeComber, P.G., "Substitutional Doping of Amorphous Silicon", *Solid State Communications*, 17, 1975, pp.1193-1196.
- Staebler, D.L., Crandall, R.S., and Williams, R., "Stability of *n-i-p* Amorphous Silicon Solar Cells", *Appl. Phys. Lett.*, 39(9), 1981, pp.733-735.
- Staebler, D.L. and Wronski, C.R., "Reversible Conductivity Changes in Discharge Produced Amorphous Silicon", *Appl. Phys. Lett.*, 31(4), 1977, pp.292-294.
- Staebler, D.L. and Wronski, C.R., "Optically Induced Conductivity Changes in Discharge-produced Hydrogenated Amorphous Silicon", *J. Applied Physics*, 51(6), 1980, pp.3262-3268.
- Street, R.A., "Trapping Parameters of Dangling Bond in Hydrogenated Silicon", *Appl. Phys. Lett.*, 41(11), 1982, pp.1060-1062.
- Street, R.A., "Transient Photoconductivity Studies of the Light Soaked State of Hydrogenated Amorphous Silicon", *Appl. Phys. Lett.*, 42(6), 1983, pp.507-509.
- Stutzmann, M., Jackson, W.B., and Tsai, C.C., "Light-induced Metastable Defects in Hydrogenated Amorphous Silicon: A Systematic Study", *Physical Review B.*, 32(1), 1985, pp.23-47.
- Suehrcke, H. and McCormick, P.G., "The Diffuse Fraction of Instantaneous Solar Radiation", *Solar Energy*, 40, 5, 1988, pp.423-430.
- Swartz, G.A., "Computer Model of Amorphous Silicon Solar Cell", *J. Applied Physics*, 53(1), 1982, pp.712-719.
- Swinbank, W.C., "Long-Wave Radiation from Clear Skies", *Quarterly Journal of the Royal Meteorological Society*, 89, 1963.
- Tawada, Y., Nishimura, K., Nonomura, S., Okamoto, H., and Hamakawa, Y., "Analysis of Photo-induced Changes in the Performance of Amorphous Silicon Solar Cells", *Solar Cells*, 9, 1983, pp.53-61.
- Temps, R.C. and Coulson, K.L., "Solar Radiation Incident upon Slopes of Different Orientations", *Solar Energy*, 19, 1977, pp.179-184.
- TRNSYS, A Transient Simulation Program, Version 12.1, Solar Energy Laboratory, University of Wisconsin, Madison, Wisconsin, 1983, pp.4.16-9.

- Tsuda,S., Nakamura,N., Watanabe,K., Takahama,T., Nishiwaki,H., Ohnishi,M., and Kuwano,Y., "Light-induced Instability of Amorphous Silicon Photovoltaic Cells", *Solar Cells*, 9, 1983, pp.25-36.
- Uchida,Y., Nishiura,M., Sakai,H., and Haruki,H., "Stability of *p-i-n* Hydrogenated Amorphous Silicon Solar Cells to Light Exposure", *Solar Cells*, 9, 1983, pp.3-12.
- Ullal,H.S., Morel,D.L., Willett,D.R., Kanani,D., Taylor,P.C., and Lee,C., "Temperature Effects and Degradation Mechanisms of *p-i-n* Thin Film Si:H Solar Cells," *Conf. Rec. of the 17th IEEE Photovoltaic Specialists Conf.*, 1984, pp.359-363.
- Willet,D.R., Private Communications, ARCO Solar Inc., From March to July, 1989.
- Xi,J.P., Tsuo,Y.S., Trefny,J.U., and McMahon,T.J., "Differences in Cell Behavior after Light Soaks through the *p*-layer and the *n*-layer of *a-Si:H p-i-n* Cells", *Conf. Rec. of the 18th IEEE Photovoltaic Specialists Conf.*, 1985, pp.519-522.
- Yamaguchi,M., Yamagishi,H., Kondo,M., Hosokawa,Y., Tsuge,K., Nakayama,T., Mizukami,S., and Tawada,Y., "Study of Electron Transport and Light-induced Effects in *a-Si:H* Films", *Conf. Rec. of the 19th IEEE Photovoltaic Specialists Conf.*, 1987, pp.845-850.
- Yanagisawa,T., "Temperature Dependence of Light-induced Degradation in *a-Si:H* Solar Cells", *Solar Cells*, 22, 1987, pp.125-132.